

# AutoEnRichness: A hybrid empirical and analytical approach for estimating the richness of galaxy clusters

Matthew C. Chan<sup>1</sup> and John P. Stott<sup>1</sup>

*E-mails:* [m.c.chan@lancaster.ac.uk](mailto:m.c.chan@lancaster.ac.uk) and [j.p.stott@lancaster.ac.uk](mailto:j.p.stott@lancaster.ac.uk)

<sup>1</sup>*Department of Physics, Lancaster University, Lancaster, LA1 4YB, UK*

Accepted XXX. Received YYY; in original form ZZZ

## ABSTRACT

We introduce AutoEnRichness, a hybrid approach that combines empirical and analytical strategies to determine the richness of galaxy clusters (in the redshift range of  $0.1 \leq z \leq 0.35$ ) using photometry data from the Sloan Digital Sky Survey Data Release 16, where cluster richness can be used as a proxy for cluster mass. In order to reliably estimate cluster richness, it is vital that the background subtraction is as accurate as possible when distinguishing cluster and field galaxies to mitigate severe contamination. AutoEnRichness is comprised of a multi-stage machine learning algorithm that performs background subtraction of interloping field galaxies along the cluster line-of-sight and a conventional luminosity distribution fitting approach that estimates cluster richness based only on the number of galaxies within a magnitude range and search area. In this proof-of-concept study, we obtain a balanced accuracy of 83.20 per cent when distinguishing between cluster and field galaxies as well as a median absolute percentage error of 33.50 per cent between our estimated cluster richnesses and known cluster richnesses within  $r_{200}$ . In the future, we aim for AutoEnRichness to be applied on upcoming large-scale optical surveys, such as the Legacy Survey of Space and Time and *Euclid*, to estimate the richness of a large sample of galaxy groups and clusters from across the halo mass function. This would advance our overall understanding of galaxy evolution within overdense environments as well as enable cosmological parameters to be further constrained.

**Key words:** galaxies: clusters: general – methods: statistical – methods: observational – methods: data analysis – techniques: photometric

## 1 INTRODUCTION

Galaxy clusters are the densest conglomerations of galaxies to have assembled in the Universe, containing tens to thousands of individual galaxies. The study of galaxy clusters is extremely important in astrophysics and cosmology research. For example, examining the mass profile of overdense environments (e.g. Carlberg et al. 1997; Geller et al. 1999; Biviano & Girardi 2003; Pointecouteau et al. 2005; Voigt & Fabian 2006; Johnston et al. 2007; Sanderson & Ponman 2010; Umetsu et al. 2011; Rines et al. 2013); understanding the evolution of large scale structure throughout cosmic time (e.g. Davis et al. 1985; Castander et al. 1995; Tsai & Buote 1996; Huss et al. 1999; Carlberg et al. 2000; Kneissl et al. 2001; Wilson 2003; Cohn & White 2005; Kravtsov & Borgani 2012) or mapping the distribution of clusters within the Universe (e.g. Davis et al. 1982; Bahcall 1988; de Lapparent 1994; Carlstrom et al. 2002; Refregier 2003; Weinberg 2005; Van Waerbeke et al. 2013; Planck Collaboration et al. 2014; Dannerbauer et al. 2019). It would be beneficial for future studies if reliable, accurate and scalable methods are developed that can provide mass estimates for a large sample of clusters.

Historically, in order to estimate the mass of clusters, researchers have regularly turned to optical surveys for determin-

ing cluster richness, where cluster richness can provide a proxy of cluster mass such that the number of galaxies within a cluster is expected to scale with cluster mass. For example, the Abell catalogue (Abell 1958) was the first comprehensive large scale cluster catalogue to establish a measurement system for cluster richness, where cluster richness was defined as the number of galaxies counted within a specific radius and between two magnitude limits (i.e. the bright limit is the magnitude of the third brightest cluster galaxy whilst the faint limit is two magnitudes dimmer than the magnitude of the third brightest cluster galaxy). Similarly, the Zwicky catalogue (Zwicky et al. 1961) was another comprehensive large scale cluster catalogue that established its own measurement system for cluster richness, where cluster richness was defined as the number of galaxies counted within an isopleth (i.e. the apparent boundary where the cluster density is twice that of the field density) and also between two magnitude limits (i.e. the bright end limit is the magnitude of the brightest cluster galaxy whilst the faint end limit is three magnitudes dimmer than the magnitude of the brightest cluster galaxy). We note that our definition of richness in this paper is the number of cluster galaxies up to an absolute magnitude faint-end  $r$  filter limit of  $-20.5$  and within an  $r_{200}$  radius.

In more recent times, a variety of automated methods have

arXiv:2208.11944v1 [astro-ph.CO] 25 Aug 2022

been developed that enable cluster mass or richness to be estimated without the need for extensive manual processing, such as utilising linking algorithms within redshift space (e.g. Huchra & Geller 1982; Yang et al. 2005; Calvi et al. 2011; Farrens et al. 2011; Wen et al. 2012; Tempel et al. 2016; Rodriguez & Merchán 2020), employing template fitting algorithms within colour-magnitude space (e.g. Postman et al. 1996; Kepner et al. 1999; Koester et al. 2007; Dong et al. 2008; Szabo et al. 2011; Rykoff et al. 2014) or training machine learning algorithms on observational/simulated measurements to indirectly estimate cluster mass (e.g. Ntampaka et al. 2019; Cohn & Battaglia 2019; Ho et al. 2019; Gupta & Reichardt 2020; Yan et al. 2020; de Andres et al. 2022; Lin et al. 2022).

Alternative approaches to determine cluster mass commonly include X-ray, caustic and weak lensing methods. From which, X-ray methods assume that the intracluster gas within a cluster is under hydrostatic equilibrium in order to calculate the cluster mass required to produce the observed X-ray emissions, based on X-ray temperature and surface brightness measurements (e.g. Balland & Blanchard 1995; Ettori et al. 2013; Amodeo et al. 2016); caustic methods assume a cluster has spherical symmetry in order to calculate the cluster mass required to generate an estimated average escape velocity for cluster galaxies, based on galaxy position and velocity measurements (e.g. Diaferio & Geller 1997; Diaferio et al. 2005; Alpaslan et al. 2012); whilst weak lensing methods make no physical assumptions about a cluster to estimate the cluster mass required to produce the observed gravitational lensing of light from background objects, based on light distortion and magnification measurements (e.g. Hoekstra et al. 2013; van Uitert et al. 2016; McClintock et al. 2019). Although, these methods have somewhat time-consuming and expensive prerequisites (e.g. conducting deep X-ray observations, requiring complete spectroscopic analysis, obtaining high quality image data for performing weak lensing analysis), whereas methods involving optical photometry are typically quicker and cheaper to obtain and analyse the resultant data.

We note that determining cluster richness from the direct counting galaxies within a cluster is limited by the projection effect (Frenk et al. 1990; van Haarlem et al. 1997; Reblinsky & Bartelmann 1999; Costanzi et al. 2018; Sunayama et al. 2020), where van Haarlem (1996) estimated that approximately one third of the clusters in the Abell catalogue may have had their richnesses severely misestimated due to contamination from the projection effect. This effect arises when foreground or background galaxies are in the same line-of-sight as the cluster itself, which means it is difficult to accurately associate galaxies to a cluster unless spectroscopic redshifts for each galaxy are known. However, this is time-consuming especially when working with large sample sizes, as it is dependent on the preciseness of the distance measurement required.

In the literature, various statistical and non-statistical background subtraction methods have been utilised to address the projection effect when obtaining counts of cluster galaxies without the need for distance measurements. One typical way is to count the number of field galaxies within a known control field sample, which can be used as a direct reference to subtract a proportional number of galaxies from a cluster's overall population to account for field galaxies (e.g. Kodama et al. 2001; Stott et al. 2007; Wylezalek et al. 2014). Another way is to define an annuli around the apparent outer perimeter of a cluster, which assumes that the annuli is far enough away to likely not contain cluster galaxies, such that a proportional number of galaxies can be subtracted from a cluster's overall population to account for field galaxies (e.g. Popesso et al. 2005; Goto et al. 2003; Popesso et al. 2004). A further approach is to establish colour cuts for differentiating between

cluster and field galaxies, where most of the galaxies within a cluster will appear to have similar colours especially if they are at the same redshift (i.e. red-sequence galaxies), whilst galaxies in the field will appear more randomised in terms of colour, especially if they are at different redshifts (e.g. Boué et al. 2008; Owers et al. 2017; Strazzullo et al. 2019). However, the approaches described here may not provide a robust or precise enough background subtraction, which is essential for accurately estimating cluster richnesses, due to these methods either being statistical or not assessing the true membership status of each cluster galaxy.

For this paper, we describe in detail a novel hybrid method, nominally known as AutoEnRichness, to perform background subtraction and estimate cluster richnesses by employing a multi-stage machine learning algorithm and a conventional luminosity distribution fitting approach respectively. The first key stage of our hybrid method involves training the multi-stage machine learning algorithm to differentiate between cluster and field galaxies. This approach is completely data-driven to automatically capture underlying relationships for maximising the accuracy of cluster galaxy identification. The second key stage of our hybrid method involves learning the best fit parameters for a luminosity distribution fitting function to enable the estimation of cluster richness from the luminosity distribution of individual clusters. This approach has a strong theoretical basis that depends only on the brightness of the cluster galaxy population within a given search radius of a cluster. Our proposed strategy will be beneficial to provide researchers in the field with well-founded estimates of cluster richness as well as consistency and robustness against line-of-sight effects to mitigate severe contamination.

We present this paper with the following structure. Firstly, in §2 we divide our methodology into five subsections, where §§2.1 describes the preparation of a photometric dataset to train a background subtraction model; §§2.2 describes the mechanisms of a multi-stage machine learning algorithm that is used as our background subtraction model; §§2.3 describes our strategy for establishing a scaling relation to estimate  $r_{200}$  of clusters; §§2.4 describes the preparation of a photometric dataset to train a luminosity distribution fitting function and §§2.5 describes the mechanisms of a luminosity distribution fitting function to estimate cluster richness. In §3 we outline our results across three subsections, where §§3.1 describes the model tuning analyses of our learned background subtraction model, scaling relation and luminosity distribution fitting function; §§3.2 describes the overall performance of our methodology on unseen clusters in various test sets and §§3.3 describes the importance of input features to our background subtraction model. Lastly, §4 discusses our findings and §5 summarises this paper.

We assumed the following  $\Lambda$ CDM cosmological parameters  $H_0 = 71 \text{ km s}^{-1} \text{ Mpc}^{-1}$ ,  $\Omega_m = 0.27$  and  $\Omega_\Lambda = 0.73$ .

## 2 METHODOLOGY

A brief outline of our multi-stage method to estimate the richness of a cluster can be seen in Figure 1. From which, the following subsections will describe our workflow in more detail.

### 2.1 Preparation of a photometric dataset to train a background subtraction model

To train our background subtraction model, we employed cluster galaxies that were identified by the Szabo et al. (2011) clus-

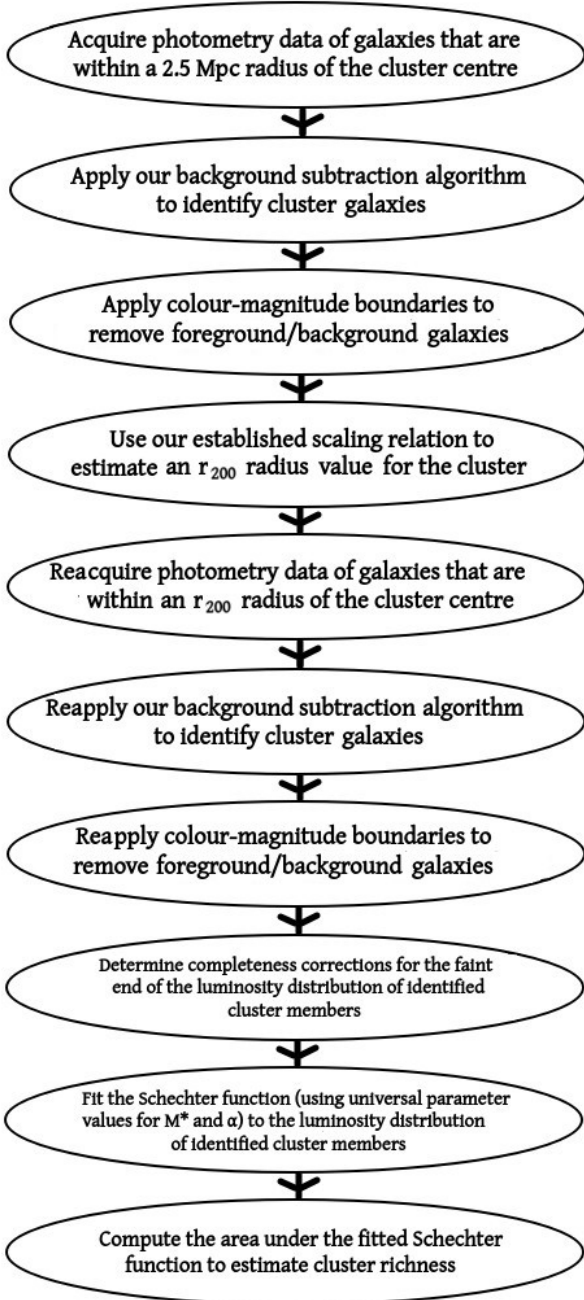


**Figure 1.** This figure shows a flowchart of the various steps in our multi-stage method to estimate the richness of a cluster, where the start of the flowchart is the first step whilst the end of the flowchart is the last step.

ter catalogue (hereafter we refer to this cluster catalogue as the AMF11 catalogue) with an estimated photometric redshift between  $0.1 \leq z \leq 0.35$ . We note that the AMF11 catalogue applied matched filters<sup>1</sup> to galaxies observed in the Sloan Digital Sky Survey Data Release 6 (SDSS-II DR6, Adelman-McCarthy et al. 2008), where clusters were detected from maximising the likelihood of the matched filters whilst cluster galaxy membership identification was based on the proximity of the galaxy from the cluster

<sup>1</sup> The matched filters were constructed from modeling positional, brightness and redshift information of cluster and field galaxy distributions.

center within  $r_{200}$ <sup>2</sup> as well as whether the likelihood difference (i.e. the difference in likelihood of detecting a cluster with and without the presence of the galaxy) was above a specified threshold. The reason we decided to use the cluster galaxies from the AMF11 catalogue was because they assessed the cluster membership status of each galaxy based on their contribution to a combination of various cluster profiles (i.e. radial surface density, luminosity and redshift). In addition, their selection method does not discriminate between ‘blue’ and ‘red’ cluster galaxies, which means it is representative of different galaxy types in clusters.

We cross-matched these cluster galaxies with galaxies observed in the Sloan Digital Sky Survey Data Release 16 (SDSS-IV DR16, Ahumada et al. 2020) to obtain the following fifteen features that are based on SDSS-IV DR16 photometry<sup>3</sup>:  $u, g, r, i, z, u-g, g-r, r-i, i-z, u-r, g-i, r-z, u-i, g-z$  and  $u-z$ . For a cluster galaxy to be successfully cross-matched, the input astronomical coordinates must be within 1 arcsecond from the astronomical coordinates of a galaxy within SDSS-IV DR16 as well as satisfying additional observing flags. These flags are as follows: the observed object should be a ‘primary’ observation<sup>4</sup> and must be classified as a galaxy object type by the SDSS photometric pipeline. We also ensured that our cluster galaxy sample only contained galaxies with a unique SDSS object identifier to prevent accidentally including galaxies that may have been selected multiple times within our search radius due to very small angular separation between overlapping line-of-sight galaxies and errors in the astrometry. In addition, we did not include cluster galaxies that were within 1646 arcseconds (i.e. 3 Mpc at  $z = 0.1$ ) of a subsample (see §2.3 for further details) of cross-matched<sup>5</sup> clusters from the Wen & Han (2015) cluster catalogue (hereafter we refer to clusters from this catalogue as WH15 clusters) and Rykoff et al. (2014) cluster catalogue (hereafter we refer to clusters from this catalogue as redMaP-Per clusters). This ensured that these clusters remained unseen for later usage in §2.3. Furthermore, we applied a cut within colour-magnitude space (i.e. if greater than the 99.75th percentile in  $r$  and  $g-r$ ) to remove any cluster galaxies that still appeared to have spurious photometry. It should be noted that throughout this work, we used  $r$  and  $g-r$  to visualise cluster and field galaxies in colour-magnitude diagrams due to  $g-r$  straddling the 4000Å break of cluster galaxies in our working redshift range.

Correspondingly, we also required a field galaxy<sup>6</sup> sample to train our background subtraction model to differentiate between cluster and field galaxies. However, we were unable to find a sizable catalogue containing identified field galaxies. This meant that we had to manually search for ‘field’ regions that did not visually appear to contain clusters from the full WH15 and redMaP-

<sup>2</sup> We refer to  $r_{200}$  as the radius containing a mean density that is two hundred times greater than the critical density of the Universe.

<sup>3</sup> We employed full-sky dust reddening maps (Schlegel et al. 1998; Schlafly & Finkbeiner 2011) to account for galactic extinction.

<sup>4</sup> We note that SDSS uses the term ‘primary’ to refer to the best imaging observation recorded for a survey object if it was seen multiple times during an observing run in an SDSS plate, whilst other observations of the object are known as ‘secondary’.

<sup>5</sup> This involved identifying clusters that were within 70 arcseconds (i.e. 250 kpc at  $z = 0.225$ ) of each other in astronomical coordinate space and within  $\pm 0.04(1+z)$  (see Wen et al. (2009) for further explanation) of each other in redshift space. In addition, the clusters had to be observed within SDSS-IV DR16 between a redshift range of  $0.1 \leq z \leq 0.35$ .

<sup>6</sup> We refer to interloping galaxies along a clusters line-of-sight as field galaxies.



Per cluster catalogues. This resulted in the identification of forty different ‘field’ regions, where the resultant astronomical sky map displaying the position of clusters and our proposed ‘field’ regions can be seen in Figure S1 (available online). We sampled galaxies from SDSS-IV DR16 that were within these ‘field’ regions. This involved applying a 1372 arcseconds (i.e. 2.5 Mpc at  $z = 0.1$ ) search radius on each of the ‘field’ regions as well as reusing the same observing flags mentioned earlier within this section to obtain our field galaxy sample. The astronomical coordinates and number of observed field galaxies for each ‘field’ region are provided in Table 1. We did not include field galaxies that were within 10 arcseconds from the cluster galaxies in the AMF11 catalogue to remove cluster galaxies that may have accidentally been included as part of the field regions. We also did not include field galaxies that were within 1646 arcseconds (i.e. 3 Mpc at  $z = 0.1$ ) of the same subsample of cross-matched WH15 and redMaPPer clusters mentioned earlier within this section to ensure that the clusters remained unseen for later usage in §2.3. Furthermore, we removed any field galaxies that were not within the same region of colour-magnitude space as our cluster galaxy sample, based on the observed minimum and maximum values for the cluster galaxies in  $r$  and  $g - r$ . This was intended to encourage our background subtraction model to learn to be more proficient at classifying galaxies with similar photometric properties. Subsequently, this yielded a total of 83315 field galaxies that had the same fifteen photometry features as our cluster galaxy sample. For this paper, we assumed that these field galaxies can be considered as ‘actual’ field galaxies.

We decided to set the redshift values of galaxies in our cluster and field galaxy samples to be based only on the photometric redshifts estimated by SDSS-IV DR16. This would enable a more straightforward comparison between the redshift distributions of both samples if they were measured via the same approach. We note that SDSS-IV DR16 applied the kd-tree nearest neighbor fit algorithm (see Csabai et al. (2007) for further details) to estimate the photometric redshifts of individual galaxies. We also used their estimated photometric redshifts to further constrain galaxies within our cluster galaxy sample to only be between a redshift range of  $0.1 \leq z \leq 0.35$ , whereas galaxies within our field galaxy sample were not redshift restricted to mimic field galaxies appearing along the line-of-sight of clusters. Although, we note that galaxies were not required to have photometric redshifts available to be included in our field galaxy sample. In addition, we computed the  $r$  filter absolute magnitudes for the cluster and field galaxies based on their photometric redshifts and corresponding K corrections<sup>7</sup>.

We note that our background subtraction model will learn to identify all cluster galaxies between a redshift range of  $0.1 \leq z \leq 0.35$ , which may result in overcounting of cluster galaxies within a cluster if there are other clusters along the line-of-sight. To limit this effect, we decided to establish colour-magnitude boundaries within colour-magnitude space when applying our background subtraction model. These boundaries are designed to capture the majority of the population of cluster galaxies at specific redshifts. We first computed the median values of  $r$  and  $g - r$  for cluster galaxies in our cluster galaxy sample across redshift intervals of  $\pm 0.005$  that are centered in redshift bins from 0.105 to 0.345 with step sizes of 0.01, as shown in Figure 2. We then manually determined appropriate

<sup>7</sup> In order to estimate the amount of K correction required, we performed linear interpolation between redshift and  $r$  filter K corrected values determined from a simple stellar population model (see Bruzual & Charlot (2003) for further details).

Right ascension (degrees)	Declination (degrees)	Number of observed galaxies
5.10408	21.0611	4488
5.77875	2.30955	7049
9.14699	33.7121	4030
10.4395	-3.84934	5377
21.3533	-3.02485	5595
23.0452	30.3202	5664
26.0012	23.8818	5024
28.3683	20.8955	2748
29.8579	11.0895	5108
38.6421	-8.10943	5168
113.919	28.0332	5223
115.323	15.458	6310
121.916	0.109439	5518
129.971	51.2851	4753
143.518	63.0839	4564
144.097	47.3992	4929
158.633	56.6154	5982
166.196	20.0867	5861
177.951	65.8863	5733
196.86	15.2355	5885
207.127	65.0462	5711
214.632	3.77235	6109
219.239	62.0499	6009
226.958	54.9023	5346
231.26	-0.0179	6696
235.973	18.662	7669
236.823	39.221	6421
238.422	58.5216	6760
255.233	18.8401	6079
263.834	28.0521	3565
316.524	-6.36219	6273
316.54	-1.56952	5201
326.258	-6.56724	6597
332.263	28.8328	4580
332.498	19.5978	4043
333.873	24.14	4214
340.098	4.71022	4252
353.561	33.6502	4239
357.0789	-4.69765	5103
359.369	17.4744	5809

**Table 1.** This table contains the astronomical coordinates (J2000) and number of observed galaxies that were sampled from our forty different proposed ‘field’ regions using a 1372 arcseconds (i.e. 2.5 Mpc at  $z = 0.1$ ) search radius. We note that the number of observed galaxies does not include field galaxies that were within 10 arcseconds of the galaxies in our cluster galaxy sample nor did we include field galaxies that were within 1646 arcseconds (i.e. 3 Mpc at  $z = 0.1$ ) of a subsample of cross-matched WH15 and redMaPPer clusters.

lower and upper boundaries of  $r_{median} - 0.01 \leq r_{median} \leq r + 0.4$  and  $g - r_{median} - 0.05 \leq g - r \leq g - r_{median} + 0.4$  for each redshift bin. This would result in ‘L-shaped’ boundaries around the cluster galaxies at a given redshift, where an example of the ‘L-shaped’ boundaries for cluster galaxies at  $z = 0.225$  is shown in Figure 3. We then applied these colour-magnitude boundaries to our cluster galaxy sample across redshift bin sizes of 0.01 to remove any cluster galaxies that were not within the colour-magnitude boundaries at their respective redshift. Subsequently, this yielded a total of 60663 cluster galaxies that were available to train our background subtraction model. For this paper, we assumed that these cluster galaxies can be considered as ‘actual’ cluster galaxies.

In Figure S2 (available online), it can be seen that our cluster

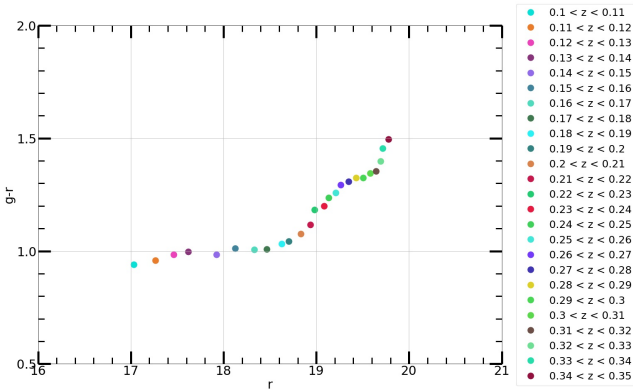


**Figure 2.** This figure shows a colour-magnitude diagram (using apparent magnitudes) of the median  $r$  and  $g-r$  for cluster galaxies at different redshift intervals from our cluster galaxy sample.

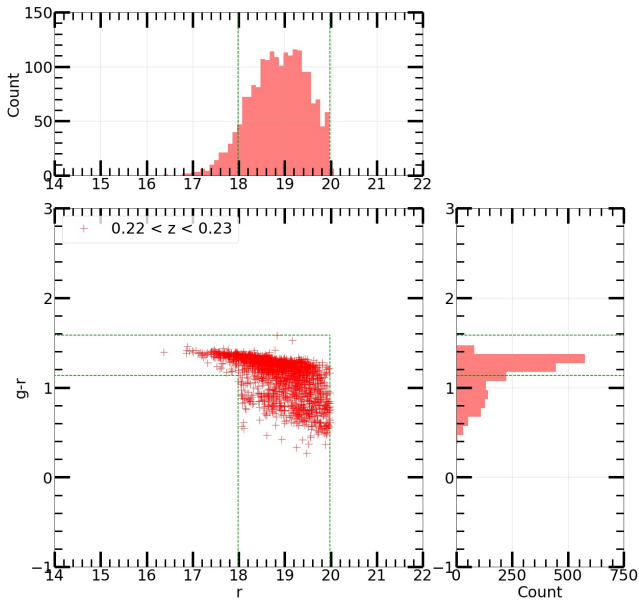


**Figure 3.** This figure shows an example of the colour-magnitude boundaries (green dotted lines) for cluster galaxies (red cross) between  $0.22 < z < 0.23$  from our cluster galaxy sample, where only galaxies that are between the colour-magnitude boundaries will be considered as part of a cluster at that redshift.

and field galaxies were taken from different areas across SDSS-IV DR16. This meant that our cluster and field galaxy samples were likely to be representative of the whole population of cluster (between a redshift range of  $0.1 \leq z \leq 0.35$ ) and field galaxies. Moreover, in Figures 4, S3 and S4 (available online), it can be seen that our field galaxy sample had an overall noticeable disparity to our cluster galaxy sample within colour-magnitude space. This somewhat validated our approach for obtaining the field galaxies given the underlying differences in photometry between the majority of the cluster and field galaxies. Although, we also observed some overlap of the ‘blue’ and faint cluster galaxies with bright field galaxies. We expect that it may be more difficult for our background subtraction model to differentiate between the galaxy classes within these overlap regions of colour-magnitude space. Furthermore, in Figure 5 we display the photometric redshift,  $r$  filter apparent magnitude and  $r$  filter absolute magnitude distributions of galaxies in

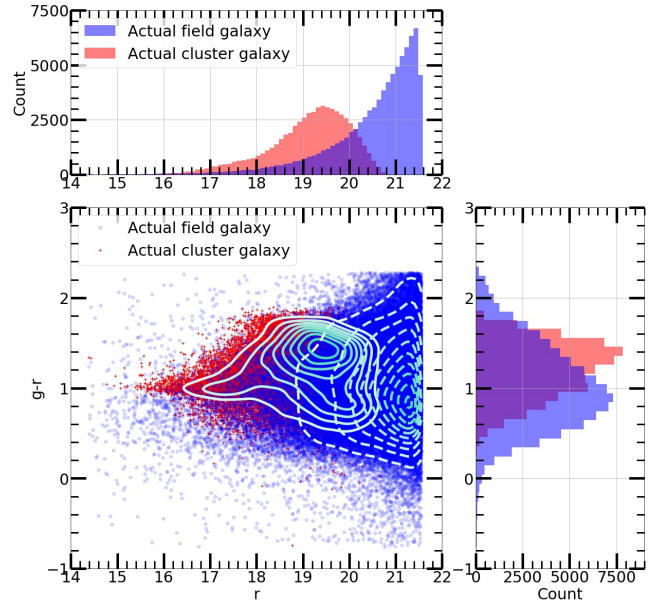


**Figure 4.** This figure shows colour-magnitude diagrams (using apparent magnitudes) of the cluster (red cross) and field (blue circle) galaxies in our cluster and field galaxy samples that were observed within SDSS-IV DR16. The non-dashed contour lines represent the density of data points for cluster galaxies whilst the dashed contour lines represent the density of data points for field galaxies.

our cluster and field galaxy samples. It can be seen that we had fewer cluster and field galaxies at lower redshifts when compared to those at higher redshifts. This indicated that we would need to sample equally across different redshifts to prevent our background subtraction model from being biased towards any particular redshift. We note that the number of field galaxies decreased significantly after  $z = 0.4$  due to the observing limitations of SDSS-IV DR16 at higher redshifts, where SDSS-IV DR16 had a  $r$  filter limiting magnitude of 22.2. We also noticed that there was a gradual drop in the number of cluster and field galaxies towards fainter magnitudes due to the incompleteness of cluster galaxies in the AMF11 catalogue and observing limitations of SDSS-IV DR16 respectively.

Finally, we partitioned our cluster and field galaxy samples into three different subsets, known as the training, validation and test sets. In particular, the training set would be used to train our background subtraction model, the validation set would be used to tune its hyper-parameters and the test set would be used to obtain an unbiased estimate of the predictive performance of our background subtraction model. This involved randomly selecting 450, 150 and 150 cluster galaxies within fixed redshift bin sizes of 0.01 across a redshift range of  $0.1 \leq z \leq 0.35$  to be within our training, validation and test sets, which resulted in a total of 11250, 3750 and 3750 cluster galaxies respectively. We also randomly selected 33750, 11250 and 11250 field galaxies to be within our training, validation and test sets respectively. It should be noted that we applied sampling weights<sup>8</sup> when selecting field galaxies to be within

<sup>8</sup> The amount of sampling weightage applied to each field galaxy in our training and validation sets was based on the resultant likelihood of the  $r$  filter apparent magnitude for the field galaxy under a normal distribution that was constructed from the mean and standard deviation of the  $r$  filter apparent magnitudes of cluster galaxies in our training and validation sets.

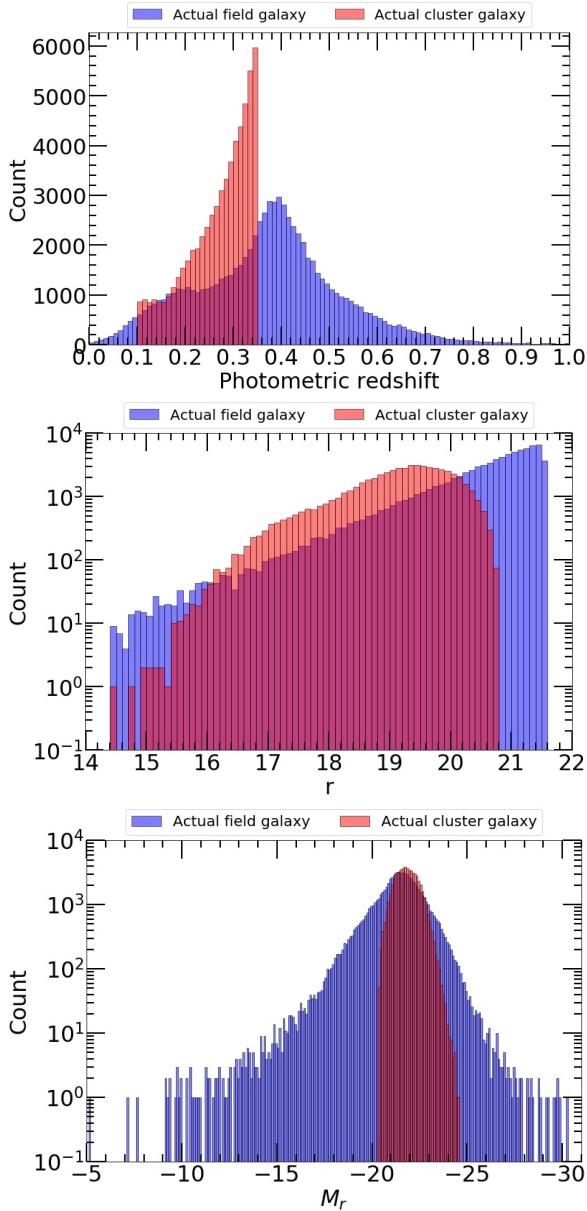


**Figure 5.** This figure shows histograms of the photometric redshift (top image),  $r$  filter apparent magnitude (middle image) and  $r$  filter absolute magnitude (bottom image) of galaxies in our cluster (red) and field (blue) galaxy samples after being cross-matched with galaxies observed within SDSS-IV DR16, where the cluster galaxies had to be between a redshift range of  $0.1 \leq z \leq 0.35$ . It should be noted that we only display field galaxies that had an available photometric redshift in the top and bottom images.

our training and validation sets to ensure that the  $r$  filter apparent magnitudes of the field galaxies overlapped with the  $r$  filter apparent magnitudes of the cluster galaxies. This would expose our background subtraction model to a larger proportion of the more difficult instances (i.e. cluster and field galaxies that had very sim-

We also shifted the computed means by  $-1$  in our training and validation sets to ensure that the cluster and field galaxy distributions overlapped at all  $r$  filter apparent magnitudes. In addition, we note that sampling with replacement was used when selecting field galaxies to be within our training and validation sets.

ilar photometry) during its training. Furthermore, we wanted our training, validation and test sets to remain as realistic as possible. As such, we permitted the number of field galaxies to outnumber (i.e. we assumed that having three field galaxies for every cluster galaxy was appropriate) the number of cluster galaxies with these sets. Although, we only permitted random sampling (i.e. equal sampling weightage) of field galaxies in our test set. These properties can be seen in Figure 6.

## 2.2 Using a multi-stage machine learning algorithm to perform background subtraction

We employed an unsupervised deep learning algorithm, known as an autoencoder (AE, Rumelhart et al. 1985), as the first stage of our background subtraction model. Our overall objective for using an AE is to train it to learn to accurately reconstruct input data. The mechanism behind the AE can be separated into three main stages, that are known as the encoder network, bottleneck and decoder network. The overall architecture for a typical AE is shown in Figure 7.

The encoder network is composed of fully-connected layers that are responsible for processing an input dataset by performing nonlinear transformations of the input data into a compressed representation. This is achieved by decreasing the number of nodes in the fully-connected layers as the size of the encoder network increases. The compression is maximised within the bottleneck, where the number of nodes in the bottleneck determines the amount of compression. The underlying objective of the bottleneck is to obtain the lowest dimensional representation of the data that captures the most generalisable aspects about the data. From which, the compressed data is then passed to the decoder network for reconstruction. This involves decompressing the compressed data back into its original input dimensionality by increasing the number of nodes in the fully-connected layers as the size of the decoder network increases. If the AE is properly trained, the reconstructed feature values should closely resemble the feature values of the input data. Overall, an AE can be considered as a type of dimensionality reduction-based algorithm since it focuses on reducing the dimensionality of the input data. However, we reconfigure its functionality from a dimensionality reduction-based algorithm into an outlier detection algorithm by also examining the differences between the reconstructed outputs and the input data. We note that the decoder network has the same but reversed architecture to the encoder network, where the number of nodes in the fully-connected layers increases rather than decreases as the size increases.

In order to train the AE to generate accurate reconstructions, we used the mean squared error as our loss function. This measured the similarity between all of the input and reconstructed feature values of galaxies via the following equation:

$$\text{Mean Squared Error} = \frac{1}{n} \sum_{i=1}^n (y_i - \hat{y}_i)^2, \quad (1)$$

where  $n$  is the number of input features,  $y$  is the input feature values and  $\hat{y}$  is the reconstructed feature values.

We set the batch size, learning rate, optimiser algorithm<sup>9</sup> and architecture layout<sup>10</sup> to be tunable hyper-parameters, where the full hyper-parameter search space is shown in Table 2.

<sup>9</sup> We recommend the reader to refer to Ruder (2016) for an overview of different optimiser algorithms.

<sup>10</sup> We considered the number of nodes in the bottleneck to be the most

Tunable hyper-parameter name	Hyper-parameter search space
Batch size	256 or 512 or 1024 or 2048
Learning rate	0.0001 or 0.001 or 0.01 or 0.1
Optimiser algorithm	Adaptive Moment Estimation (Adam) or Adaptive Delta (Adadelta) or Adaptive Gradient Optimiser (Adagrad) or Adam Based On The Infinity Norm (Adamax) or Adam With Nesterov Momentum (Nadam) or Stochastic Gradient Descent (SGD) or Root Mean Squared Propagation (RMSprop)
Architecture layout (number of nodes and hidden layers in the encoder network and bottleneck)	<b>1</b> (13 nodes in first hidden layer, 11 nodes in second hidden layer, 9 nodes in third hidden layer, 7 nodes in the fourth hidden layer and 1 node in the bottleneck) or <b>2</b> (13 nodes in first hidden layer, 11 nodes in second hidden layer, 9 nodes in third hidden layer, 7 nodes in the fourth hidden layer and 3 nodes in the bottleneck) or <b>3</b> (13 nodes in first hidden layer, 11 nodes in second hidden layer, 9 nodes in third hidden layer, 7 nodes in the fourth hidden layer and 5 nodes in the bottleneck)

**Table 2.** This table contains a list of tunable hyper-parameters for the AE as well as the range of values that were explorable in the hyper-parameter space via random search. We also set a maximum of ten thousand trainable epochs as well as enabling early stopping of the model training if the validation loss had not decreased by 0.001 over fifty epochs from the best observed validation loss. Furthermore, we again remind the reader that the encoder and decoder networks had reversed symmetrical designs, so we did not specify the number of nodes or hidden layers for the decoder network within this table.

We employed a separate machine learning algorithm, known as logistic regression (see [Morgan & Teachman \(1988\)](#) for further details), as the second stage of our background subtraction model. This served to convert the outputs of the AE into class predictions. In particular, we used the known class labels as the target variable and the mean squared error between the input and reconstructed feature values as the input variable, where if an input was poorly reconstructed by the AE then the corresponding mean squared error will be large too. From which, the logistic regression algorithm determines whether a galaxy should be classified as a cluster or field galaxy (i.e. the galaxy class with the higher predicted probability) when given the mean squared error of each galaxy. In this work, we decided to use the defaulted hyper-parameter values for the logistic regression algorithm (N.B. without regularisation) in the `SCIKIT-LEARN` ([Pedregosa et al. 2011](#)) machine learning library since we primarily wanted to examine the influence of the AE in our background subtraction model. We expect that tuning the hyper-parameters for the logistic regression algorithm may slightly improve the overall predictive performance of our background subtraction model but this can be explored further in future work. It should be noted that the logistic regression algorithm minimised the following loss function during its training:

$$\text{Log Loss} = -\frac{1}{n} \sum_{i=1}^n y_i \log(p_i) + (1 - y_i) \log(1 - p_i), \quad (2)$$

where  $n$  is the number of inputs,  $y$  is the true class value (i.e. either 0 or 1) and  $p$  is the predicted probability (i.e. between 0 and 1) of being a galaxy class. This loss function measured the difference between predicted probability and true class value of galaxies.

We utilised a random search (see [Bergstra & Bengio \(2012\)](#)

significant component of an AE's architecture since it is influential in the amount of generalization learned. We decided that the number of nodes in the bottleneck should be a tunable hyper-parameter whilst the number of nodes for the hidden layers in the encoder and decoder networks would remain fixed.

for further details) strategy to examine the predictive performance of our background subtraction model with different hyper-parameter combinations, where random search is a computationally efficient approach that does not need to examine every hyper-parameter combination. Instead, it considers that hyper-parameter optimization can be characterised by a Gaussian process, such that only a minority of hyper-parameter combinations are actually important. For example, we can assume that a randomly selected hyper-parameter combination has a ninety-five per cent probability of being situated within the top five per cent of all possible hyper-parameter combinations from the optimum after conducting only sixty iterations of random search. At the same time, we employed a Monte Carlo cross-validation (see [Morgan & Teachman \(1988\)](#) for further details) strategy to examine the variability of the predictive performance of our background subtraction model with different weight initialisations and dataset compositions. This involved repeated random sampling of new training, validation and test sets over ten iterations to measure the average predictive performance across the ten iterations. Ideally, we aimed to select a hyper-parameter combination that offered consistency and good predictive performance.

To determine the optimal hyper-parameter combination of our background subtraction model, we utilised the trapezium rule to compute the area under a precision-recall curve (AUCPR, [Boyd et al. 2013](#)) for each hyper-parameter combination, which is based on the following set of equations:

$$\text{Precision} = \frac{\text{TP}}{\text{TP} + \text{FP}}, \quad (3)$$

$$\text{Recall} = \frac{\text{TP}}{\text{TP} + \text{FN}}, \quad (4)$$

$$\text{AUCPR} = \int \text{Precision } d(\text{Recall}), \quad (5)$$

where TP is the number of correctly classified 'actual' cluster galaxies, FP is the number of incorrectly classified 'actual' cluster galaxies and FN is the number of incorrectly classified 'actual'



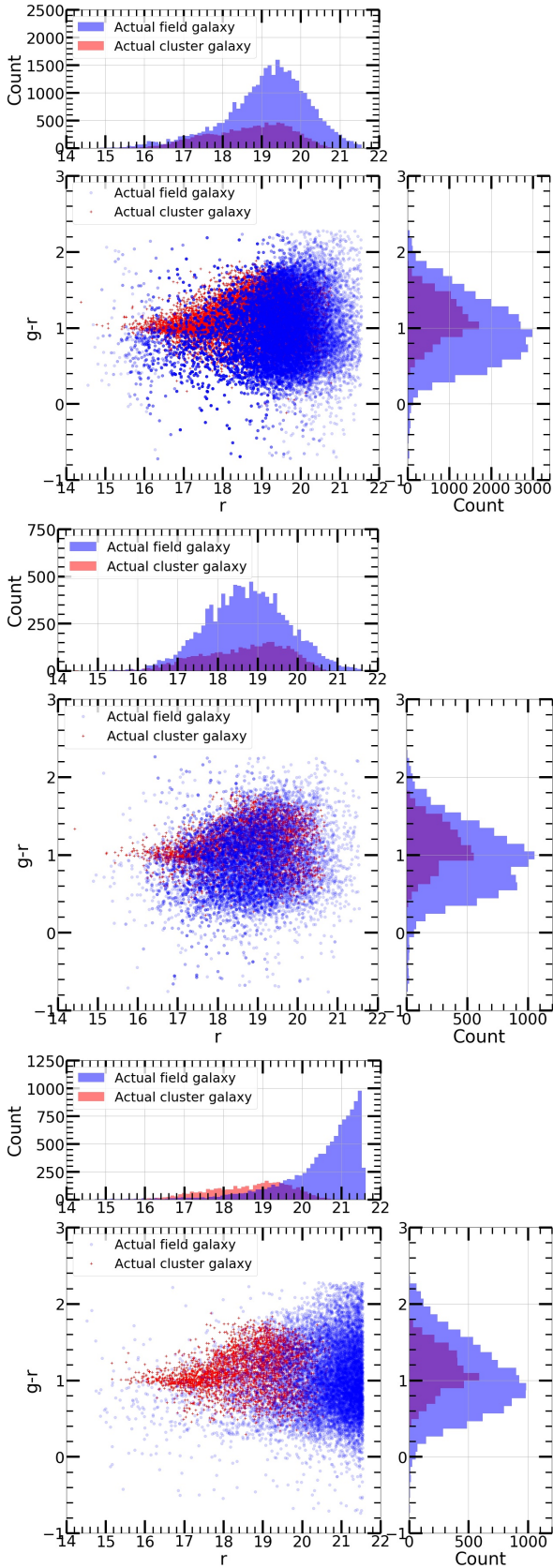


**Figure 6.** This figure shows colour-magnitude diagrams (using apparent magnitudes) of the cluster (red cross) and field (blue circle) galaxies in our training (top image), validation (middle image) and test (bottom image) sets that were observed within SDSS-IV DR16.

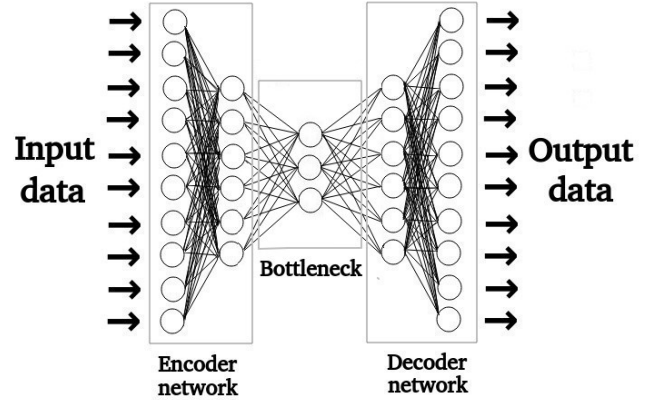


**Figure 7.** This figure shows an example of the architecture layout for a typical AE. The AE is composed of three main stages that are known as the encoder network, bottleneck and decoder network, where the nodes in each hidden layer are fully-connected to the nodes of the adjacent hidden layers. We also employed a rectified linear unit (ReLU, [Nair & Hinton 2010](#)) activation function with ‘He uniform’ ([He et al. 2015](#)) weight initialisation for each hidden layer in the encoder network, bottleneck and decoder network, whilst a linear activation function with ‘Glorot uniform’ ([Glorot & Bengio 2010](#)) weight initialisation was used for the output layer of the decoder network. In addition, we initialised all biases to zeros. It should be noted that we utilised the KERAS deep learning framework ([Chollet et al. 2015](#)) to construct the AE.

field galaxies. Briefly, this metric measured the proportion of predictions that were predicted as cluster galaxies as well as the proportion of ‘actual’ cluster galaxies that were recovered across all class probability thresholds. It is ideal for assessing the predictive performance of a model that focuses on correctly identifying ‘rare’ instances (i.e. when there is a class imbalance). The optimal hyper-parameter combination would maximise the AUCPR for galaxies in our validation set.

Next, we determined the corresponding optimal class probability threshold when using the optimal hyper-parameter combination. This involved comparing the F1 score ([Lipton et al. 2014](#)) yielded for each class probability threshold (i.e. from 0 to 1 with class probability threshold step sizes of 0.01) via the following equation:

$$\text{F1 Score} = 2 \left( \frac{\text{Precision} \times \text{Recall}}{\text{Precision} + \text{Recall}} \right). \quad (6)$$

This metric was similar to AUCPR in functionality except it only considered the predictive performance at a specific class probability threshold. The optimal class probability threshold would maximise the F1 score for galaxies in our validation set.

Lastly, we determined the overall classification accuracy of our background subtraction model at distinguishing between cluster and field galaxies in our test set. This involved computing the balanced accuracy ([Brodersen et al. 2010](#)) when using the optimal class probability threshold and optimal hyper-parameter combination via the following equation:

$$\text{Balanced Accuracy} = \frac{1}{2} \left( \frac{\text{TP}}{\text{TP} + \text{FN}} + \frac{\text{TN}}{\text{TN} + \text{FP}} \right), \quad (7)$$

where TP is the number of correctly classified ‘actual’ cluster galaxies, TN is the number of correctly classified ‘actual’ field galaxies, FP is the number of incorrectly classified ‘actual’ cluster



galaxies and FN is the number of incorrectly classified ‘actual’ field galaxies. The primary advantage of using balanced accuracy rather than conventional classification accuracy is that balanced accuracy takes into account class imbalance whereas conventional classification accuracy assumes equal class sizes when measuring the predictive performance of a binary classification model.

### 2.3 Establishing a scaling relation to estimate $r_{200}$

It is beneficial to measure the richness of clusters within a characteristic radius (e.g.  $r_{200}$ ,  $r_{500}$ ,  $r_{2500}$ ) because it enables a more straightforward comparison of cluster richness across different cluster catalogues. We decided to establish a scaling relation that predicts values for the characteristic radius of cross-matched WH15 and redMaPPer clusters from §§2.1. We note that WH15 used a friend-of-friend grouping algorithm on galaxies with known spectroscopic or photometric redshifts to identify clusters in the Sloan Digital Sky Survey Data Release 12 (SDSS-III DR12, Alam et al. 2015) whilst redMaPPer used a red-sequence fitting algorithm on galaxies within colour-magnitude space to identify clusters in the Sloan Digital Sky Survey Data Release 8 (SDSS-III DR8, Aihara et al. 2011). Subsequently, we obtained a total of 6064 cross-matched WH15 and redMaPPer clusters between a redshift range of  $0.1 \leq z \leq 0.35$ . We decided to use these clusters because they were found via two conventional approaches for cluster detection. This enabled us to directly compare the consistency of richness estimates from using our novel cluster galaxy identification technique versus other cluster galaxy identification techniques. In this proof-of-concept study, we choose to employ only a subsample of 1000 cross-matched WH15 and redMaPPer clusters when creating our scaling relation for time efficiency.

We also decided to use  $r_{200}$  as our characteristic radius since the cluster galaxies in our training and test sets from the AMF11 catalogue were originally sampled within  $r_{200}$ . In particular, we utilised  $r_{200}$  values that were estimated by WH15 as the dependent variable in our scaling relation, where their  $r_{200}$  estimates were computed via a scaling relation between  $r_{200}$  measurements from X-ray/weak lensing observations and total luminosity in the  $r$  band of all the identified cluster galaxies. For this work, we assumed that these  $r_{200}$  values can be considered as ‘actual’  $r_{200}$  values. In Figure S5 (available online), we noticed that there was a strong linear relationship between WH15<sup>11</sup> and redMapper richness<sup>12</sup>. This means that we can directly compare our predicted richnesses with the richness estimates of redMaPPer. Furthermore, we noticed that there was a non-linear relationship between  $r_{200}$  and both WH15 and redMaPPer richnesses which was in accordance with the empirical richness-size relation observed in Hansen et al. (2005), where our ‘actual’  $r_{200}$  values appeared to have greater variability at lower richnesses. As such, we expected that our scaling relation would have greater variability in  $r_{200}$  at lower richnesses too.

We then partitioned the cross-matched WH15 and redMaPPer

<sup>11</sup> We refer to the  $R_{L^*}$  variable from the WH15 catalogue as WH15 richness, where they computed cluster richness by measuring the total luminosity of identified galaxy members as a function of the typical luminosity of galaxies in the  $r$  filter.

<sup>12</sup> We refer to the  $\lambda/S$  variable from the redMaPPer catalogue as redMaPPer richness, where they computed cluster richness by determining an expected richness which would yield the observed projected density,  $i$  filter magnitudes and multiple colour indices of the identified red-sequence galaxies.

clusters into a training set and test set. We nominally referred to these sets as the CMWR (i.e. cross-matched WH15 and redMaPPer) training and test sets to avoid confusion with the training and test sets created in §§2.1. The purpose of having the CMWR training set was to determine the best fit coefficients of our scaling relation whilst the purpose of having the CMWR test set was to measure the predictive performance of our learned scaling relation. Since we knew the spectroscopic redshift of the CMWR clusters, we segmented them into fixed redshift bin sizes of 0.01. This ensured that our training and test sets contained clusters from across the redshift scale via stratified sampling<sup>13</sup>. This involved randomly allocating approximately half of the clusters within each redshift bin into both sets, which resulted in our CMWR training and test sets containing 500 clusters each. The spectroscopic redshift and richness distributions of clusters in our CMWR training and test sets can be seen in Figure 8.

Next, we applied a search radius of 2.5 Mpc at each cluster’s spectroscopic redshift as well as reapplying the same observing flags mentioned in §§2.1 to acquire galaxies from SDSS-IV DR16. This gave us a total of 2020690 galaxies, where our CMWR training set consisted of 1005167 galaxies and our CMWR test set consisted of 1015523 galaxies. We then applied our background subtraction model and colour-magnitude boundaries to count the number of cluster galaxies within each cluster. We established a linear scaling relation that was based on the number of identified cluster galaxies as an independent variable and  $r_{200}$  as the dependent variable. This involved learning the best fit coefficients by minimising the residual sum of squares between the dependent and independent variables in a linear regression algorithm from the SCIKIT-LEARN machine learning library, where we again used the defaulted hyperparameter values for the linear regression algorithm. We note that our cross-matched WH15 and redMaPPer cluster sample contained many clusters with low richness but only a few clusters with high richness. As such, we decided to assign the WH15 richness of each cluster as individual weights in the linear regression algorithm to minimise the effect of overfitting to potential outliers from clusters with low richness.

### 2.4 Preparation of a photometric dataset to estimate individual cluster richnesses

In order to measure richness within  $r_{200}$  of individual clusters, we first approximated  $r_{200}$  for clusters in our CMWR training and test sets using the learned scaling relation from §§2.3 to reacquire galaxies within  $r_{200}$  from SDSS-IV DR16. We nominally referred to these new sets as the CMWR- $r_{200}$  training and test sets to avoid confusion with the CMWR training and test sets created in §§2.3. Similar to before, the purpose of having the CMWR- $r_{200}$  training set was to determine the best fit coefficients of a luminosity distribution fitting function whilst the purpose of having the CMWR- $r_{200}$  test set was to measure the predictive performance of the learned luminosity distribution fitting function. We obtained a total of 299807 galaxies in our CMWR- $r_{200}$  training set and 306953 galaxies in our CMWR- $r_{200}$  test set. The resultant color-magnitude diagrams of galaxies in our CMWR- $r_{200}$  training and test sets is shown in Figure 9.

<sup>13</sup> Stratified sampling is a strategy that minimises selection bias by splitting a dataset into new distributions that approximately resemble the original distribution.

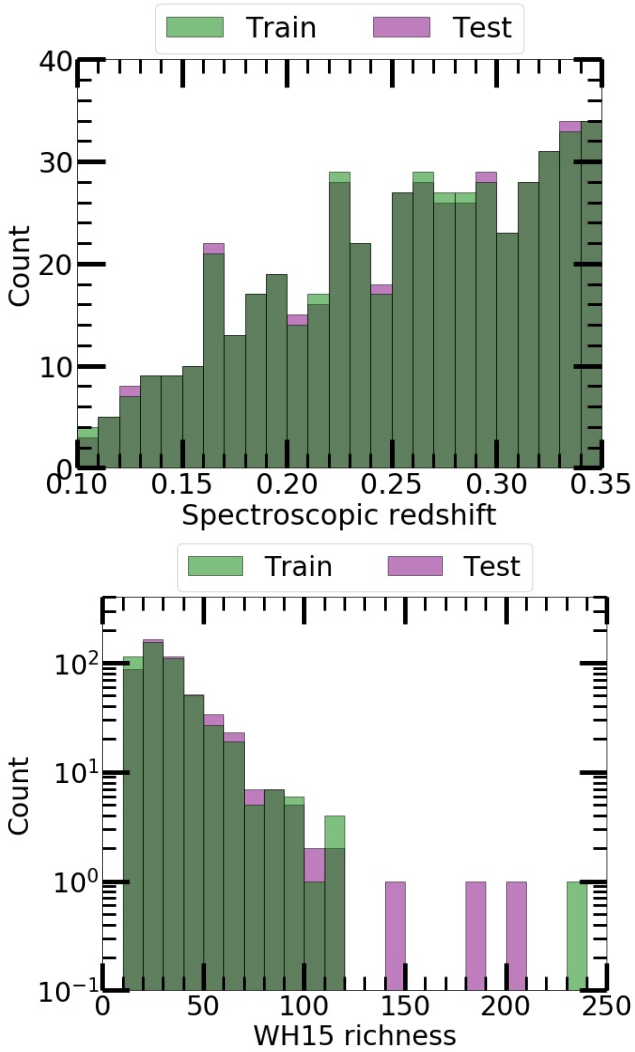


**Figure 8.** This figure shows histograms of the cluster spectroscopic redshift (top image) and WH15 richness (bottom image) distributions of clusters in our CMWR training (green) and test (purple) sets that were between a redshift range of  $0.1 \leq z \leq 0.35$ .

### 2.5 Using a luminosity distribution fitting function to estimate individual cluster richnesses within $r_{200}$

We adopted a similar approach to the methodology described in [Schechter \(1976\)](#) to estimate the richness of individual clusters. [Schechter \(1976\)](#) showed that it was possible to use a luminosity distribution fitting function (i.e. the Schechter function) to do this. Briefly, this involved fitting the function to a composite luminosity distribution of cluster galaxies in order to determine best fit parameter values of the function. Then [Schechter \(1976\)](#) assumed that the best fit parameter values for  $M^*$  and  $\alpha$  can be applied universally to the luminosity distribution of individual clusters to locally fit for  $n^*$  and thus estimate cluster richness. The Schechter function is expressed via the following equation:

$$n(M)dM = [0.4 \ln(10)] n^* [10^{0.4(M^* - M)}]^\alpha e^{-10^{0.4(M^* - M)}} dM, \quad (8)$$

where  $M$  is absolute magnitude,  $n^*$  is the number of galaxies per unit magnitude,  $M^*$  is the ‘characteristic’ magnitude at which the distributions of faint and bright galaxies rapidly changes and  $\alpha$

is the faint end slope parameter that describes the distribution of galaxies fainter than  $M^*$ . We note that  $M^*$  and  $\alpha$  directly influence the steepness of the bright and faint ends in the Schechter function whilst  $n^*$  varies based on the observed number of galaxies within magnitude bins.

Firstly, we applied our background subtraction model and colour-magnitude boundaries to identify cluster galaxies from the CMWR- $r_{200}$  training set. We then performed Chi-squared fitting<sup>14</sup> with initialisation bounds for  $M^*$  (i.e. between  $-30$  and  $-15$ ),  $n^*$  (i.e. between 0 and positive infinity) and  $\alpha$  (i.e. between  $-2$  and  $-1$ ) when fitting the Schechter function to a composite luminosity distribution that consisted of a subsample of identified cluster galaxies which appeared to have high completeness (i.e. greater than 90 per cent when using a base-10 logarithmic scale for the counts) between a restricted  $r$  filter absolute magnitude (i.e. between  $-25$  and  $-21.5$ ) and redshift (i.e. between 0.1 and 0.15) range. At the same time, we also explored various  $r$  filter absolute magnitude bin sizes (i.e. from 0.01 to 3 with step sizes of 0.01) to obtain an optimal  $r$  filter absolute magnitude bin size that minimised the Chi-squared fitting error and yielded galaxies across five or more  $r$  filter absolute magnitude bins. Furthermore, we approximated the uncertainty in the number of identified cluster galaxies within each magnitude bin by assuming that the uncertainty followed a Poisson sampling hypothesis<sup>15</sup> when fitting the Schechter function. From which, we determined an optimal absolute magnitude bin size and best fit parameter values for  $M^*$ ,  $n^*$  and  $\alpha$ , where we also assumed that the best fit parameter values for  $M^*$  and  $\alpha$  can be applied universally to the luminosity distribution of individual clusters.

We remind the reader that our background subtraction model had not yet been corrected for the incompleteness of faint galaxies from observing limitations. This meant that we had to derive completeness corrections for the luminosity distribution (i.e. using  $r$  filter absolute magnitudes) of individual clusters at different redshifts. Initially, we grouped the identified cluster galaxies from the CMWR- $r_{200}$  training set into redshift intervals of  $\pm 0.04(1+z)$  that were centered in redshift bins from 0.105 to 0.345 with step sizes of 0.01, where identified cluster galaxies from different redshifts can go into multiple bins. Next, we fitted a 100 per cent completeness line across adjacent  $r$  filter apparent magnitude bins<sup>16</sup> that were on the bright side of the peak and within the completeness limit of the AMF11 catalogue for each redshift interval. We then approximated the completeness fraction of the faintest  $r$  filter apparent magnitude bin (N.B. we considered the two faintest magnitude bins on the bright side of the peak beyond  $z > 0.14$  and three faintest magnitude bins on the bright side of the peak beyond  $z > 0.33$  as the incompleteness of galaxies became more visibly noticeable for more

<sup>14</sup> We used the *curve fit* function from the SciPy Python library ([Virtanen et al. 2020](#)) to perform Chi-squared fitting of the Schechter function, which returned the best fit parameter values that minimised the Chi-squared fitting error and also returned an estimated covariance matrix of the best fit parameter values.

<sup>15</sup> A Poisson sampling hypothesis assumed that the distribution of galaxies is dictated by a Poisson process, such that the standard deviation of the counts within each magnitude bin was based on the square root of the count ([Schechter 1976](#)).

<sup>16</sup> We used an  $r$  filter apparent magnitude bin size that corresponded to the optimal  $r$  filter absolute magnitude bin size. In addition, when working with the luminosity distribution of individual clusters we only considered cluster galaxies within an  $r$  filter absolute magnitude range of  $-25$  to  $-20.5$ , where  $-20.5$  was the  $r$  filter absolute magnitude limit that was used to determine WH15 richness in [Wen & Han \(2015\)](#).

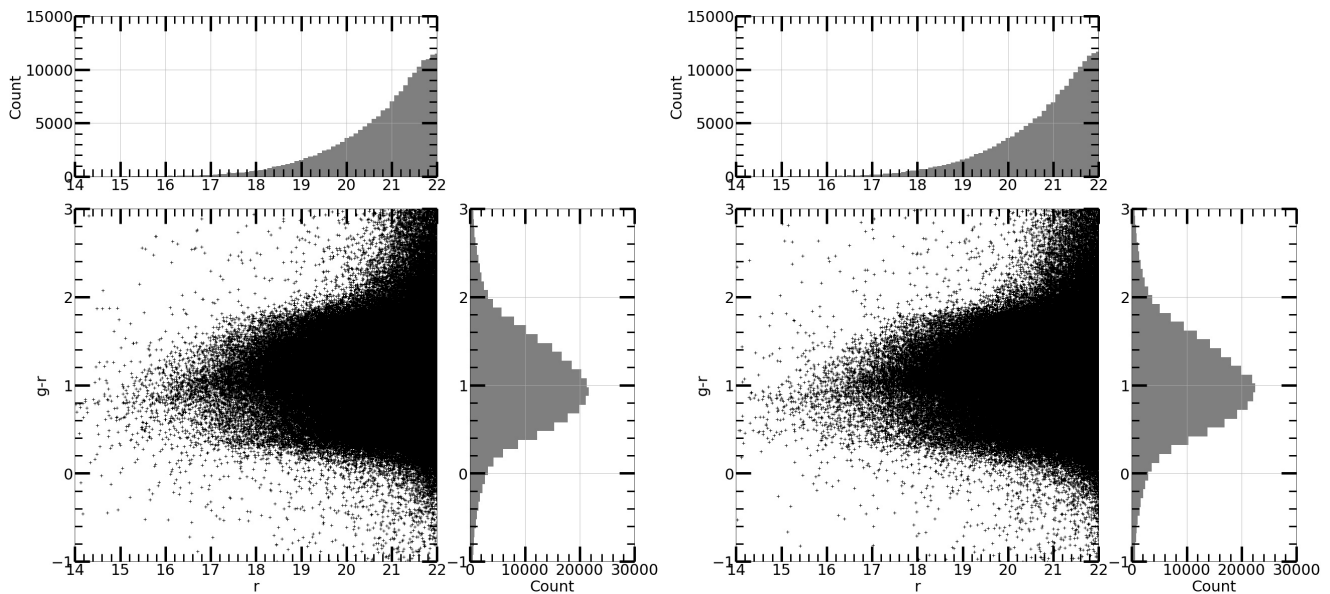


**Figure 9.** This figure shows colour-magnitude diagrams (using apparent magnitudes) of galaxies in our CMWR- $r_{200}$  training (left image) and test (right image) sets that were within an  $r_{200}$  search radius and observed within SDSS-IV DR16.

magnitude bins at higher redshifts) by calculating the fraction in the expected number of cluster galaxies (i.e. based on the 100 per cent completeness line) to the observed number of cluster galaxies (i.e. identified by our background subtraction model).

We applied these completeness fractions to the luminosity distribution of individual clusters by multiplying the observed count of the faintest (N.B. we again considered the two faintest magnitude bins on the bright side of the peak beyond  $z > 0.14$  and three faintest magnitude bins on the bright side of the peak beyond  $z > 0.33$ )  $r$  filter absolute magnitude bin<sup>17</sup> on the bright side of the peak by the completeness fraction of the corresponding  $r$  filter apparent magnitude bin within the nearest redshift interval. We then replaced the uncertainty range of the observed count in the magnitude bin with this computed completeness correction value as the new lower and upper uncertainty limits when performing Chi-square fitting. This ensured that the Schechter function did not fit to incomplete  $r$  filter absolute magnitude bins.

Finally, we estimated cluster richnesses within  $r_{200}$  by integrating<sup>18</sup> the locally fit Schechter function. This gave us the expected number of cluster galaxies within  $r_{200}$  that had an  $r$  filter absolute magnitude brighter than  $-20.5$ . We also compared our estimated cluster richnesses with WH15 richnesses, spectroscopic redshift, ‘actual’  $r_{200}$  and redMaPPer richnesses in order to examine the predictive performance of the optimal  $r$  filter absolute magnitude bin size and best fit parameters for  $M^*$  and  $\alpha$  in the Schechter function. We note that WH15 richness was specific to  $r_{200}$  whereas redMaPPer richness was specific to redMaPPer’s own scaling radius rather than  $r_{200}$ . This meant that we could directly quantify the error between our estimated cluster richnesses and WH15 richnesses by using root mean squared error as a metric.

<sup>17</sup> Since our completeness fractions were measured in  $r$  filter apparent magnitudes, we had to convert between  $r$  filter apparent magnitudes and  $r$  filter absolute magnitudes to determine the relevant completeness fraction.

<sup>18</sup> We utilised the incomplete Gamma function (see Equation 27 in Schechter (1976)) to compute the integral.

## 3 RESULTS

### 3.1 Model tuning analyses

#### 3.1.1 Analysis of our trained background subtraction model

We conducted ten iterations of Monte Carlo cross-validation to measure the variability of the predictive performance of our background subtraction model, as well as conducting sixty iterations of random search on the tunable hyper-parameters of our background subtraction model, to determine an optimal hyper-parameter combination that maximised the AUCPR of galaxies in our validation set. It can be seen in Table S1 (available online) that the optimum hyper-parameter combination was as follows: optimal batch size = 2048; optimal learning rate = 0.0001; optimal optimiser algorithm = RMSprop and optimal architecture layout = 3. This optimum hyper-parameter combination yielded a mean AUCPR value of 40.24 per cent with a standard deviation of 1.85 per cent for galaxies in our validation set. Furthermore, it can be seen in Table S2 (available online) that the optimum class probability threshold was 0.29, when using the optimum hyper-parameter combination. This optimum class probability threshold yielded a FI score of 48.92 per cent for galaxies in our validation set.

#### 3.1.2 Analysis of our established scaling relation to estimate $r_{200}$

We constructed a scaling relation using clusters in our CMWR training set to estimate the  $r_{200}$  of each cluster when given the number of cluster galaxies identified by our background subtraction model as an input. The best fit coefficients of our scaling relation were determined by minimising the weighted residual sum of squares between the independent and dependent variables, where our scaling relation is defined via the following equation:

$$\text{pred}_{r_{200}} = (3.39 \pm 0.23)n_{gal} + (950.65 \pm 25.25), \quad (9)$$

where  $\text{pred}_{r_{200}}$  is the predicted  $r_{200}$ ,  $n_{gal}$  is the number of cluster galaxies identified within a 2.5 Mpc search radius at each

cluster’s spectroscopic redshift and the uncertainty represents the standard error of the parameter estimates. In Figure 10, it can be seen that there was a larger drop in the number of cluster galaxies identified by our background subtraction model at higher redshifts (i.e.  $z > 0.3$ ) when compared to the number of identified cluster galaxies at lower redshifts with the same ‘actual’  $r_{200}$  values. This was likely due to cluster galaxies at higher redshifts having larger observed photometric errors, which made it more difficult for our background subtraction model to identify these cluster galaxies. We note that we obtained a Pearson correlation coefficient value of 0.39 between the number of identified cluster galaxies and ‘actual’  $r_{200}$  variables. We also observed that both WH15 and redMaPPer richnesses appeared to somewhat linearly increase with ‘actual’  $r_{200}$  and the number of identified cluster galaxies. Furthermore, in Figure 11, we compared the predictive performance of our predicted  $r_{200}$  with the ‘actual’  $r_{200}$ , where we found that our predicted  $r_{200}$  was quite comparable to the ‘actual’  $r_{200}$  across all cluster sizes. Although, we noticed there was greater variability in the predicted  $r_{200}$  at lower cluster richnesses, where we obtained a root mean squared error of 218.14 and a median absolute percentage error of 11.89 per cent between our predicted and ‘actual’  $r_{200}$  values.

### 3.1.3 Analysis of the best fit parameters for a luminosity distribution fitting function to estimate individual cluster richnesses Within $r_{200}$

We used a Chi-squared fitting approach to determine the best fit parameters of the Schechter function when fitting to a composite luminosity distribution that consisted of a subsample of identified cluster galaxies from our CMWR training set with high completeness. We also simultaneously determined an optimal  $r$  filter absolute magnitude bin size that minimised the Chi-squared fitting error and yielded galaxies across five or more  $r$  filter absolute magnitude bins. In Table S3 (available online), we identified an optimal  $r$  filter absolute magnitude bin size of 0.52 that had corresponding best fit parameter values of  $M^* = -22.81$  with a standard deviation of  $\pm 0.5$ ;  $n^* = 159.82$  with a standard deviation of  $\pm 154.62$  and  $\alpha = -1.99$  with a standard deviation of  $\pm 0.37$ . In Figure 12, we display the composite luminosity distribution and fitted Schechter function using the optimal  $r$  filter absolute magnitude bin size and best fit parameter values.

We then used the optimal  $r$  filter absolute magnitude bin size and best fit parameter values for  $M^*$  and  $\alpha$  to fit the Schechter function to the luminosity distribution of individual clusters from our CMWR- $r_{200}$  training set. This enabled us to estimate individual cluster richnesses by integrating the locally fit Schechter function. Subsequently, we obtained a root mean squared error of 18.06 and a median absolute percentage error of 34.33 per cent between our estimated cluster richnesses and WH15 richnesses within  $r_{200}$ . In Figure 13, we noticed that WH15 richnesses had a strong linear correlation with our estimated cluster richnesses. We also observed that spectroscopic redshifts seemed to have no distinguishable correlation with our estimated cluster richnesses. In addition, we noticed that there was a strong linear correlation between ‘actual’  $r_{200}$ , redMaPPer richnesses and our estimated cluster richnesses. These results confirmed that our approach to estimate individual cluster richnesses was appropriate since we did not train any of our models to minimise cluster richness prediction error but we still obtained strong correlations with WH15 and redMaPPer richnesses. Furthermore, we were aware that our CMWR- $r_{200}$  training set contained clusters that were not truly unseen, as we had utilised these clusters before to create our scaling relation. Although, it was still

interesting to test our methodology on clusters that were seen and unseen to compare differences in predictive performance.

## 3.2 Overall performance analyses with test sets

We further assessed our entire methodology on clusters belonging to our various test sets to obtain an unbiased evaluation of the true predictive performance of our models. Firstly, we applied our background subtraction model to cluster and field galaxies in our test set. This yielded a F1 score of 72.81 per cent and a balanced accuracy of 83.20 per cent when using the optimal hyper-parameter combination and optimal class probability threshold for our background subtraction model. In Figure 14, we display a direct comparison of the ‘actual’ and predicted cluster and field galaxies. It can be seen that our background subtraction model learned to correctly classify almost all of the field galaxies surrounding the cluster galaxies but it made more incorrect classifications in regions where the ‘actual’ cluster and field galaxies had greater overlap within colour-magnitude space. Meanwhile, in Figure 15, we compared the number of cluster and field galaxies identified by our subtraction model across redshift bin sizes of 0.01. At lower redshifts (i.e.  $z \leq 0.45$ ), we noticed that our background subtraction model slightly underestimated (i.e. misclassified ‘actual’ field galaxies as cluster galaxies or misclassified ‘actual’ cluster galaxies as field galaxies) the overall number of ‘actual’ cluster and field galaxies. In particular, we noticed a larger drop in the number of identified ‘actual’ cluster galaxies between  $0.3 \leq z \leq 0.35$ , which was similar to our observation in Figure 10. Correspondingly, at higher redshifts (i.e.  $z > 0.45$ ), we found that our background subtraction model correctly classified almost all of the galaxies. In Figures 16 and 17, we compared the number of cluster and field galaxies identified by our subtraction model across  $r$  filter apparent and absolute magnitude bin sizes of 0.1 respectively. In both magnitude distributions, we noticed that our background subtraction model slightly underestimated the overall number of ‘actual’ cluster galaxies at all magnitudes. We also noticed that our background subtraction model slightly underestimated the overall number of ‘actual’ field galaxies at intermediate brightnesses (i.e. between 16.5 and 20.5 in  $r$  filter apparent magnitude and between  $-24$  and  $-20$  in  $r$  filter absolute magnitude) but correctly classified almost all of the other fainter and brighter ‘actual’ field galaxies. Furthermore, in Figure 18 we examined the proportion of ‘red’ and ‘blue’ ‘actual’ cluster galaxies that were identified by our background subtraction model at different redshifts. We found that our background subtraction model identified 84.32 per cent of ‘red’ ‘actual’ cluster galaxies and recovered 73.11 per cent of ‘blue’ ‘actual’ cluster galaxies between a redshift range of  $0.1 \leq z \leq 0.35$ . This indicated that our background subtraction model was more confident at identifying ‘red’ ‘actual’ cluster galaxies than ‘blue’ ‘actual’ cluster galaxies, which was likely due to the ‘blue’ ‘actual’ cluster galaxies having greater overlap with field galaxies within colour-magnitude space.

We then applied our learned scaling relation and colour-magnitude boundaries to clusters in our CMWR test set to approximate  $r_{200}$  for each cluster. In Figure 19, we noticed that the number of identified cluster galaxies and ‘actual’  $r_{200}$  was relatively consistent with our learned scaling relation from Figure 10. From which, we obtained a Pearson correlation coefficient value of 0.50 between the number of identified cluster galaxies and ‘actual’  $r_{200}$  variables in Figure 19. We also noticed that our predicted and ‘actual’  $r_{200}$  values in Figure 20 was similar to the overall trend observed in Figure 11, where we obtained a root mean squared error of 200.86 and



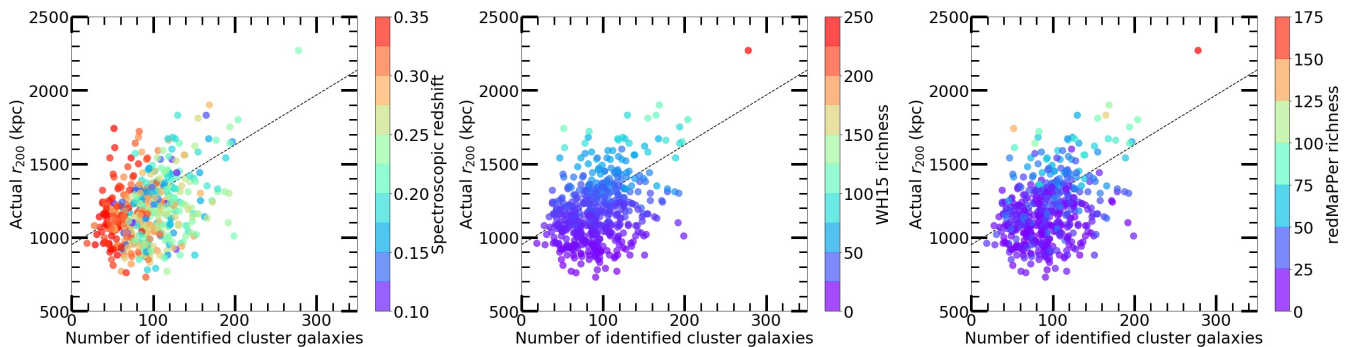


**Figure 10.** This figure shows our scaling relation (black dotted line) to estimate the  $r_{200}$  of clusters. It used the ‘actual’  $r_{200}$  of clusters from our CMWR training set as a dependent variable and the number of cluster galaxies identified by our background subtraction model within a 2.5 Mpc search radius at each cluster’s spectroscopic redshift as an independent variable. We also display the corresponding spectroscopic redshift (left image), WH15 richness (middle image) and redMaPPer richness (right image) of each cluster.

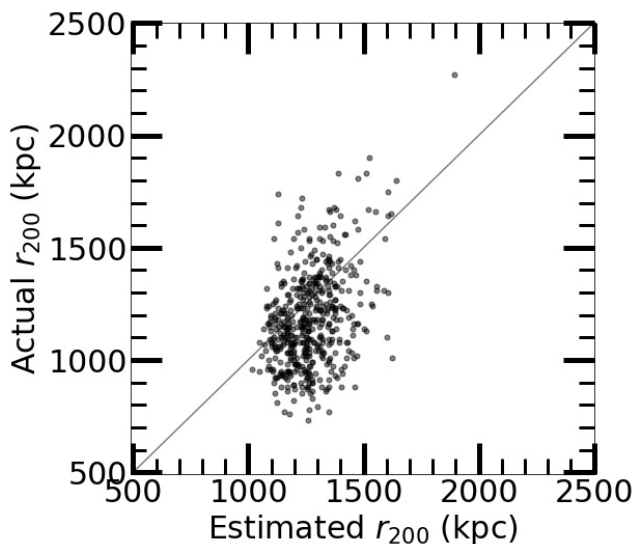


**Figure 11.** This figure shows a direct comparison of  $r_{200}$  predicted by our scaling relation with the ‘actual’  $r_{200}$  of clusters from our CMWR training set.

a median absolute percentage error of 11.66 per cent between our predicted and ‘actual’  $r_{200}$  values in Figure 20.

Finally, we examined the predictive performance of the optimal  $r$  filter absolute magnitude bin size and best fit parameter values for  $M^*$  and  $\alpha$  in the Schechter function on individual clusters in our CMWR- $r_{200}$  test set. In Figure 21, we noticed that the overall trends between our estimated cluster richnesses and WH15 richnesses with spectroscopic redshifts, ‘actual’  $r_{200}$  and redMaPPer richnesses were again consistent with Figure 13, where our estimated cluster richnesses had no distinct correlation with spectroscopic redshifts and our estimated cluster richnesses linearly increased with ‘actual’  $r_{200}$  and redMaPPer richnesses. Subsequently, we obtained a root mean squared error of 18.04 and a median absolute percentage error of 33.50 per cent between our estimated cluster richnesses and WH15 richnesses within  $r_{200}$ .

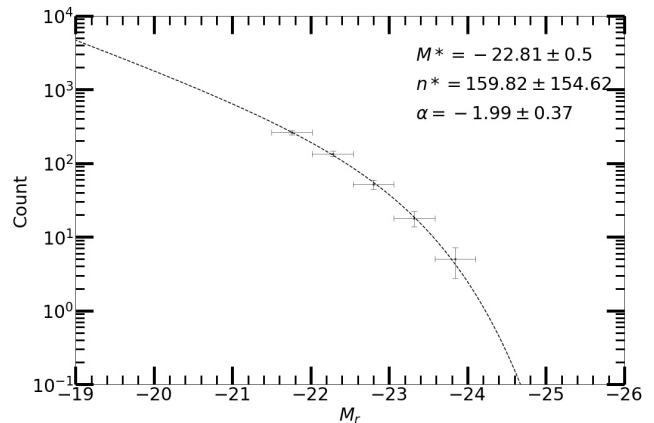


**Figure 12.** This figure shows the best fit Schechter function (black dotted line) overlaid on a composite luminosity distribution (using  $r$  filter absolute magnitudes) that consisted of a subsample of identified cluster galaxies from our CMWR- $r_{200}$  training set with an optimal  $r$  filter absolute magnitude bin size of 0.52. The best fit parameter values and their respective standard deviations are displayed in the top right corner of the figure. The x-axis error bars display the width of each  $r$  filter absolute magnitude bin and the y-axis error bars display the standard deviation of the observed count within each  $r$  filter absolute magnitude bin when assuming a Poisson sampling hypothesis.

### 3.3 Examining the importance of input features to our background subtraction model

In Figure 22, we examined the importance of each input feature to our background subtraction model. This involved randomly shuffling the data of each input feature and then applying our background subtraction model on the dataset to observe how the shuffled feature impacted the predictive performance. This strategy is known as permutation feature importance testing (Breiman 2001), where the permutation scores were based on the number of ‘actual’ cluster galaxies identified by our background subtraction model. In particular, a lower permutation score for an input feature implied greater reliance of our background subtraction model on that specific input feature to provide good predictive performance, because randomly shuffling the data for an important input feature would result in fewer ‘actual’ cluster galaxies being identified. We applied this permutation feature importance test to galaxies in our test set, which originally contained 3750 cluster galaxies. Subsequently, we

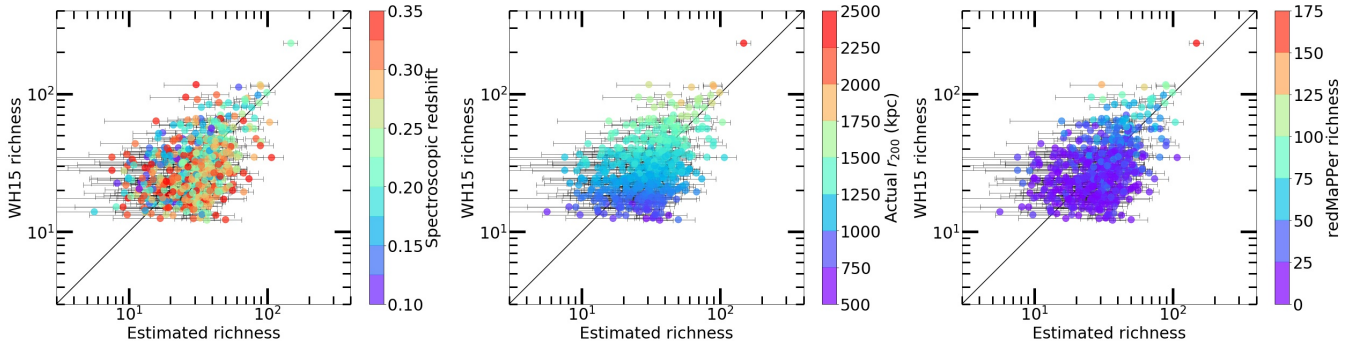


**Figure 13.** This figure shows a direct comparison between our estimated cluster richnesses and WH15 richnesses of clusters from our CMWR- $r_{200}$  training set when using the optimal  $r$  filter absolute magnitude bin size and best fit parameter values for  $M^*$  and  $\alpha$ . We also display the corresponding spectroscopic redshifts (left image), ‘actual’  $r_{200}$  (middle image) and redMaPPer richness (right image) for each cluster. The x-axis error bars display the standard deviation of the locally fit  $n^*$  when computing the integral of the Schechter function to determine our estimated cluster richnesses.

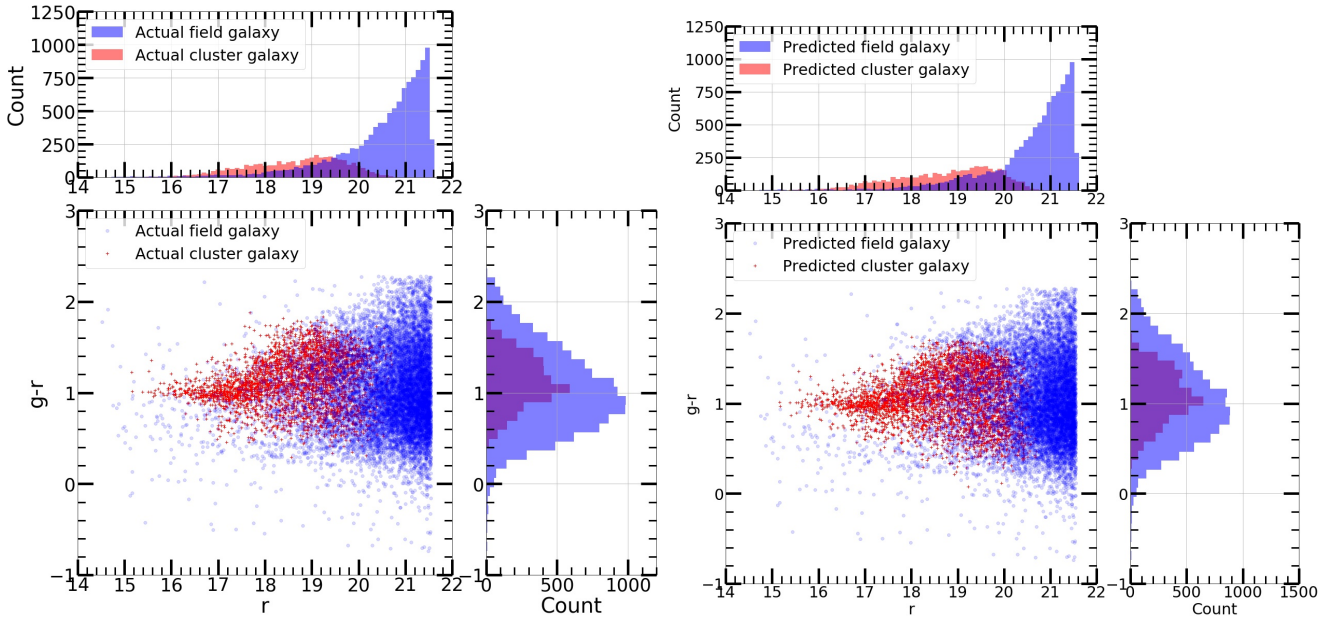


**Figure 14.** This figure shows a direct comparison of the colour-magnitude diagrams (using apparent magnitudes) for the ‘actual’ (left image) and predicted (right image) cluster (red cross) and field (blue circle) galaxies in our test set.

observed that  $g$ ,  $r$ ,  $i$ ,  $z$ ,  $u-g$ ,  $u-r$ ,  $g-i$  and  $g-z$  appeared to have greater significance to our background subtraction model whereas  $u$ ,  $g-r$ ,  $r-i$ ,  $i-z$ ,  $r-z$ ,  $u-i$  and  $u-z$  appeared to have lesser significance to our background subtraction model. Although, it is important to note that our background subtraction model had effectively utilised all the input features since the number of identified ‘actual’ cluster galaxies for each input feature was still only a fraction of the original number of ‘actual’ cluster galaxies.

#### 4 DISCUSSION

In Figure 5, we observed that the photometric redshift distribution of galaxies in our cluster galaxy sample was skewed towards higher redshifts, such that higher redshift cluster galaxies were overrepresented. To achieve a fair representation of cluster galaxies at different redshifts in our background subtraction model, we randomly sampled a fixed number of cluster galaxies within fixed redshift bin sizes of 0.01 when creating our training, validation and test sets.

This ensured that our background subtraction model was exposed to equal numbers of cluster galaxies at various redshifts within colour-magnitude space. We also exposed our background subtraction model to equal numbers of cluster and field galaxies during its training. This was to ensure a fair representation of the different galaxy classes in our background subtraction model.

We initially constrained our training sample to only spectroscopically confirmed cluster galaxies from the AMF11 catalogue but we quickly noticed that the training sample itself had a significant drop in the number of faint cluster galaxies across all redshifts when compared to the non-spectroscopically confirmed cluster galaxies. As such, we decided not to adopt this constraint when training our background subtraction model. Furthermore, we did not utilise spectroscopically confirmed field galaxies since it was difficult to acquire a sample that was representative of all potential foreground and background galaxies encountered within a random field. Although, in future work this may be possible since the num-

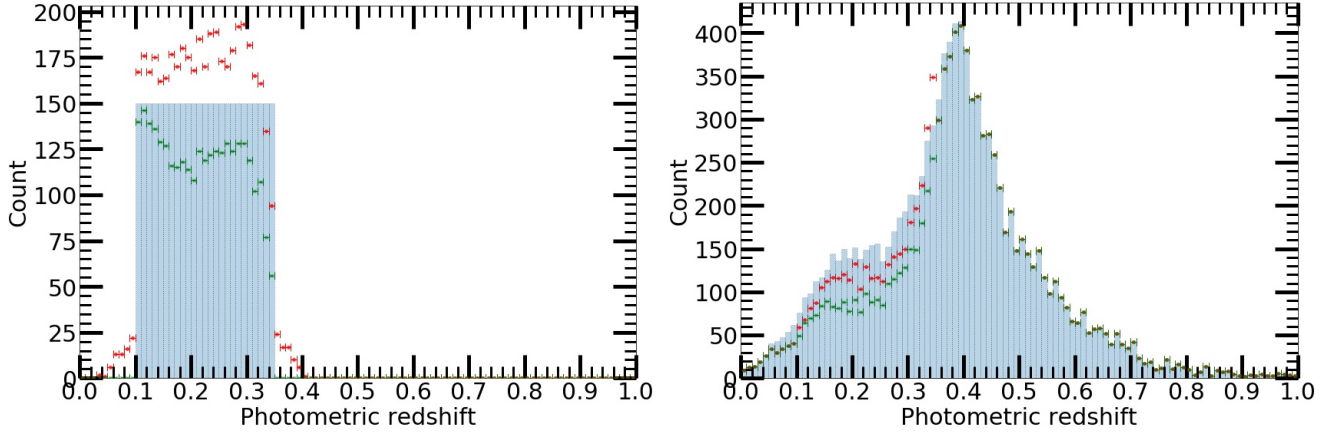


**Figure 15.** This figure shows histograms of the number of identified cluster (left image) and field (right image) galaxies in our test set when using fixed redshift bin sizes of 0.01. The blue fill with black dotted lines represents the original number of ‘actual’ cluster or field (N.B. we only display field galaxies that had an available photometric redshift) galaxies within each redshift bin. The red points represent the number of cluster or field galaxies identified by our background subtraction model within each redshift bin, the green crosses represent the number of ‘actual’ cluster or field galaxies identified by our background subtraction model within each redshift bin and the x-axis error bars display the width of each redshift bin.

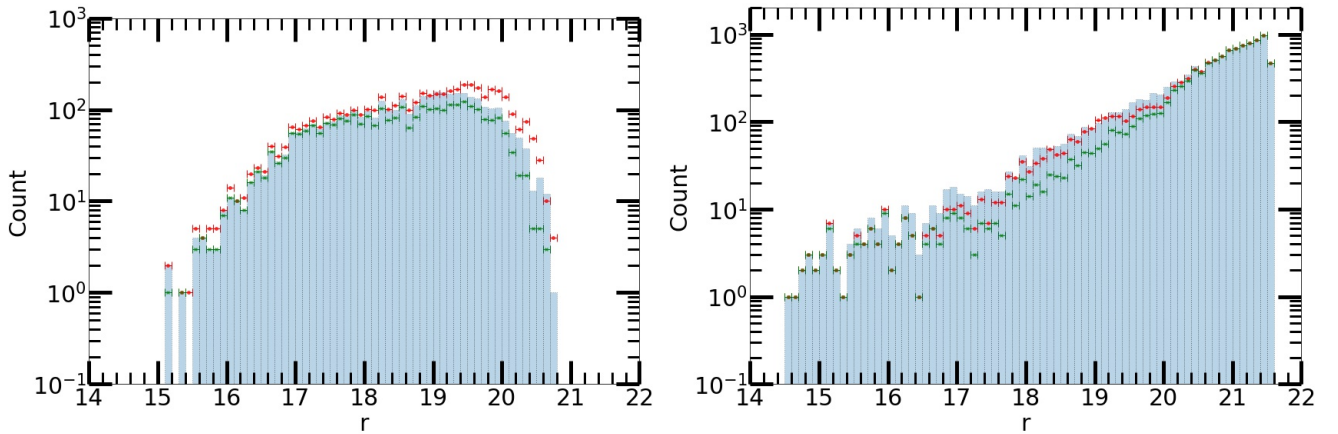


**Figure 16.** This figure shows histograms of the number of identified cluster (left image) and field (right image) galaxies in our test set when using fixed  $r$  filter apparent magnitude bin sizes of 0.1. The blue fill with black dotted lines represents the original number of ‘actual’ cluster or field galaxies within each  $r$  filter apparent magnitude bin. The red points represent the number of cluster or field galaxies identified by our background subtraction model within each  $r$  filter apparent magnitude bin, the green crosses represent the number of ‘actual’ cluster or field galaxies identified by our background subtraction model within each  $r$  filter apparent magnitude bin and the x-axis error bars display the width of each  $r$  filter apparent magnitude bin.

ber of spectroscopically confirmed cluster and field galaxies would naturally increase over time.

When constructing our scaling relation, we employed ‘actual’  $r_{200}$  values that were estimated from a scaling relation (see Equation 1 in Wen et al. (2012)) that was based on the total  $r$  filter luminosity of identified cluster galaxies within a 2.5 Mpc radius from the cluster center at each clusters redshift. This meant that the errors from their estimated  $r_{200}$  values would have carried over into our estimated  $r_{200}$  values too. In future work, we could instead consider employing  $r_{200}$  values from X-ray cluster catalogues as X-ray emission measurements are not as significantly influenced by projection effects (Ebeling et al. 2010). This would improve the overall precision of our ‘actual’  $r_{200}$  values and thus improve the precision of our cluster richness estimates within  $r_{200}$ . Furthermore, we can establish a scaling relation for any radii, not only  $r_{200}$ , as long as we have sufficient data to enable the construction of a scaling relation for the radii.

In Figures 13 and 21 we did not observe any redshift biases

in our estimated cluster richnesses after we applied completeness corrections to account for fewer observed galaxies at the faint end of the luminosity distribution of individual clusters. This indicated that incompleteness of our cluster galaxy sample from the AMF11 catalogue had a bigger impact on estimating cluster richnesses than incompleteness from misclassifications by our background subtraction model. Although, in Figures 10, 15 and 19 we observed a larger drop in the number of identified cluster galaxies at higher redshifts (i.e.  $z > 0.3$ ) when compared to the number of identified cluster galaxies at lower redshifts. We believed that this could be due to the cluster galaxies at higher redshifts having larger photometric errors than cluster galaxies at lower redshifts, which can be seen in Figure 18 by the increased scatter between data points as redshift increased. Naturally, this would make it more difficult for our background subtraction model to identify them. As such, we would expect there to be fewer cluster galaxies identified at higher redshifts, since we did not truly account for cluster galaxies having larger photometric errors at higher redshifts in our background sub-



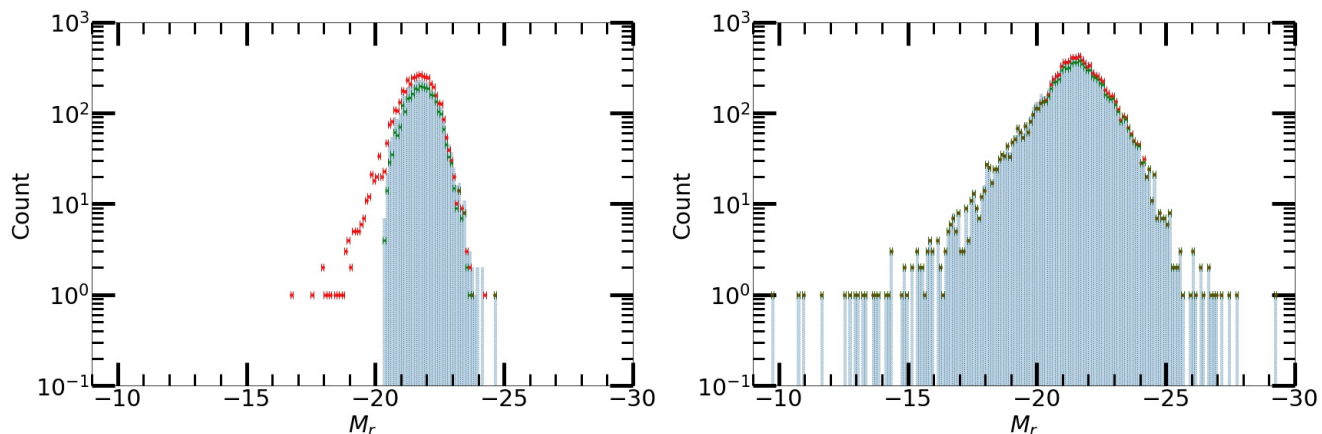


**Figure 17.** This figure shows histograms of the number of identified cluster (left image) and field (right image) galaxies in our test set when using fixed  $r$  filter absolute magnitude bin sizes of 0.1. The blue fill with black dotted lines represents the original number of ‘actual’ cluster or field (N.B. we only display field galaxies that had an available photometric redshift) galaxies within each  $r$  filter absolute magnitude bin. The red points represent the number of cluster or field galaxies identified by our background subtraction model within each  $r$  filter absolute magnitude bin, the green crosses represent the number of ‘actual’ cluster or field galaxies identified by our background subtraction model within each  $r$  filter absolute magnitude bin and the x-axis error bars display the width of each  $r$  filter absolute magnitude bin.

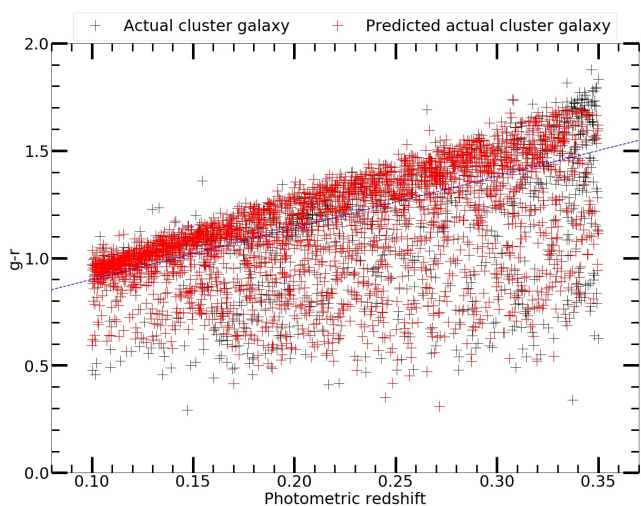


**Figure 18.** This figure shows a comparison of the ‘red’ and ‘blue’ ‘actual’ cluster galaxies (black cross) in our test set that were identified (red cross) by our background subtraction model at different redshifts, where we assumed that galaxies above the blue dashed line were ‘red’ and galaxies below the blue dashed line were ‘blue’.

traction model. In the future, it would be beneficial to obtain and utilise a larger cluster galaxy sample when training our background subtraction model, which would hopefully reduce this effect by exposing the model to more examples. It may also be beneficial to employ an algorithm that can learn to interpolate regions within colour-magnitude space in order to account for the larger photometric errors at higher redshifts, such as a variational autoencoder (Kingma & Welling 2013).

In this work, we used the Schechter function to fit to the luminosity distribution of identified cluster galaxies, where it was important to review the cluster membership status of each individual galaxy in order to minimise severe contamination from bright interloping field galaxies when fitting the Schechter function. Although, we were aware of alternative luminosity functions that could be used to fit to the luminosity distribution of cluster galaxies. Two

other commonly used luminosity functions<sup>19</sup> include the Zwicky function (Zwicky 1957) and Abell function (Abell 1975). Briefly, the Zwicky function is fitted by considering the difference in magnitude of each cluster galaxy from the brightest cluster galaxy whereas the Abell function is fitted by combining two separately fitted analytical functions. This means that the Zwicky function requires identifying the brightest cluster galaxy beforehand whereas the Abell function is not continuous at all luminosities. We decided to use the Schechter function over these other luminosity functions because the Schechter function did not have strict prerequisite conditions and offers continuity (i.e. it was composed of a power law and an exponential function) at all luminosities (Sarazin 1986).

We fitted the Schechter function to a composite luminosity distribution that consisted of a subsample of identified cluster galaxies with high completeness to obtain best fit parameter values of  $M^* = -22.81$  with a standard deviation of  $\pm 0.5$ ;  $n^* = 159.82$  with a standard deviation of  $\pm 154.62$  and  $\alpha = -1.99$  with a standard deviation of  $\pm 0.37$ . We did not allow  $\alpha$  to be greater than  $-1$  or lesser than  $-2$  when performing Chi-squared fitting, as we assumed that it would be unphysical for the number of cluster galaxies to be decreasing or increasing rapidly at fainter magnitudes respectively. We also did not set any specific bounds for  $M^*$  and  $n^*$ , since these parameters were more dependent on the given data. We attempted to compare our best fit parameter values for  $M^*$  and  $\alpha$  to the best fit parameter values of  $M^*$  and  $\alpha$  found in the literature from cluster studies to determine whether our best fit parameter values for  $M^*$  and  $\alpha$  were appropriate as ‘universal’ values. However, we found that the literature contained a wide range of values for  $M^*$  and  $\alpha$  that depended on a variety of different factors (e.g. photometric system used, magnitude range examined, redshift range examined, cluster mass range examined, composition of galaxy types in cluster sample, background subtraction method used). Although, we noticed that some typical values obtained for  $M^*$  and  $\alpha$  span approximately from  $-23$  to  $-20$  and  $-2.1$  to  $-0.8$  respectively (e.g. Oegerle et al. 1987; Oegerle & Hoessel 1989; Valotto et al. 1997;

<sup>19</sup> We recommend the reader to refer to Sarazin (1986) for an overview of different luminosity functions.



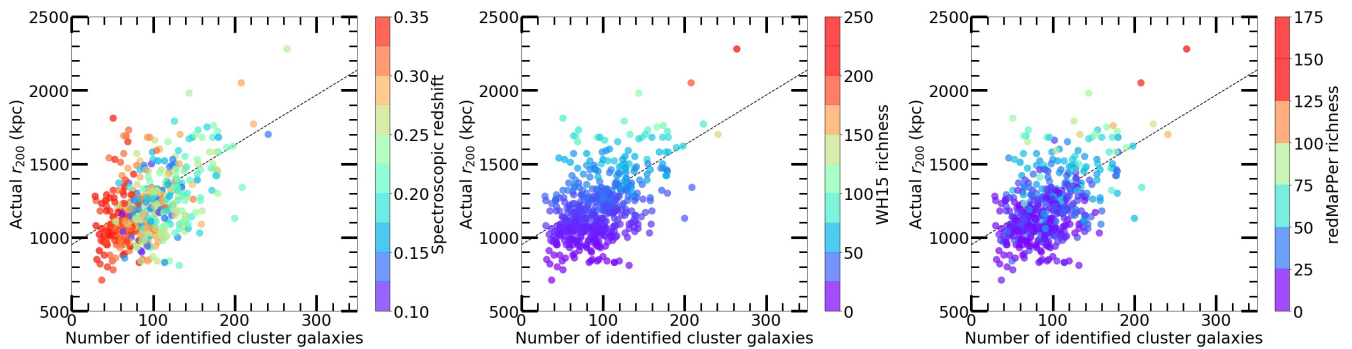


**Figure 19.** This figure is equivalent to Figure 10 except we overlaid our learned scaling relation (black dotted line) on clusters in our CMWR test set.

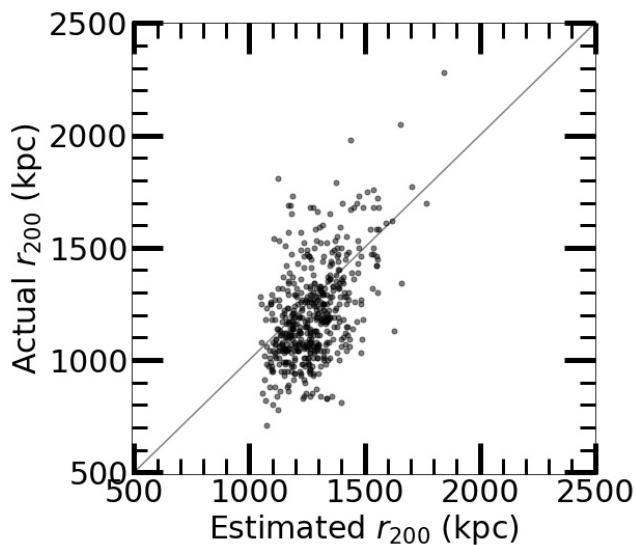


**Figure 20.** This figure is equivalent to Figure 11 except it compared the predicted and ‘actual’  $r_{200}$  of clusters in our CMWR test set.

Rauzy et al. 1998; Paolillo et al. 2001; Popesso et al. 2005). This suggested that our assumptions for  $M^*$  and  $\alpha$  were not unreasonable.

We remind the reader that our approach for estimating cluster richness was based only on the number of cluster galaxies identified by our background subtraction model within a defined magnitude range and given search area. This would be particularly beneficial for cosmological studies (Sarazin 1986), such as comparing simulated and observed halo mass functions (e.g. Castro et al. 2016; Yennapureddy & Melia 2019), since it would reduce the complexity of modeling an appropriate selection function to correct for biases from post-processing (e.g. incorrect star/galaxy classification, deblending/interpolation issues, misestimated photometric redshifts) or survey conditions (e.g. flux limitations, oversaturation by bright stars, different aperture sizes) (Melin et al. 2005). In addition, our background subtraction method provides robustness when estimating cluster richness along any line-of-sight environment since it assesses the cluster membership status of galaxies based only on their photometric measurements. This is not easily achievable when using simple statistical-based or colour-based background subtraction methods. Furthermore, our background subtraction method does not require us to make any assumptions about the properties of the cluster and field galaxies since these properties are self-learned

by the AE algorithm. This means that our background subtraction method is not intrinsically biased towards selecting different galaxy types.

In future work, it would be interesting to examine the applicability of our background subtraction method on different usage cases. These include studying the properties and evolution of identified cluster galaxies or deciding spectroscopic follow-ups of potential galaxy members in clusters or measuring the observed radial density, luminosity and redshift profiles of clusters. We also aim to extend this current work by also establishing an empirical scaling relation between our richness estimates and cluster dark matter halo masses, that have been inferred via weak gravitational lensing, in order to construct an observed halo mass function for constraining cosmological parameters. In addition, we intend to integrate our background subtraction method with our own cluster finder model (Deep-CEE, Chan & Stott 2019) and photometric redshift estimator model (Z-Sequence, Chan & Stott 2021) to mask or remove interloping line-of-sight galaxies in image data or photometric catalogue data respectively to further minimise their model predictions errors.

We note that there are various other types of conventional machine learning algorithms<sup>20</sup> available, aside from AE’s, which could be used for the task of performing background subtraction. These could include the K-nearest neighbours algorithm (Fix 1951), K-means algorithm (Macqueen 1967), isolation forest algorithm (Liu et al. 2008), support vector machine algorithm (Cortes & Vapnik 2009) and XGBoost algorithm (Chen & Guestrin 2016). The reason we chose to utilise an AE over other conventional machine learning algorithms was due to the fact that an AE is a deep neural network, which is capable of self-learning the importance of input features. On the other hand, most conventional machine learning algorithms require important features to be manually extracted in order to attain good predictive performance, which can be time-consuming and difficult to do when there are many complex features (Liang et al. 2017; Notley & Magdon-Ismail 2018; O’Mahony et al. 2019; Liu et al. 2022).

When training our background subtraction model, we used a Monte Carlo cross-validation strategy to determine an optimal hyper-parameter combination that offered the best predictive performance possible across different weight initialisations by performing random subsampling of our training and validation sets. Although, this may have resulted in some galaxies not being

<sup>20</sup> We recommend the reader to refer to <https://pyod.readthedocs.io/en/latest/pyod.models.html> for an extensive list of outlier detection algorithms (Zhao et al. 2019).

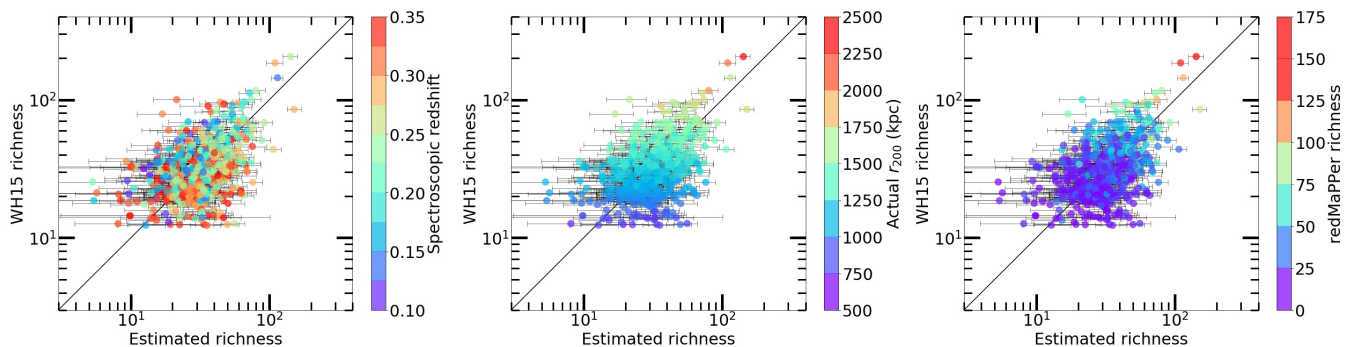


**Figure 21.** This figure is equivalent to Figure 13 except it was applied to unseen clusters from the CMWR- $r_{200}$  test set.

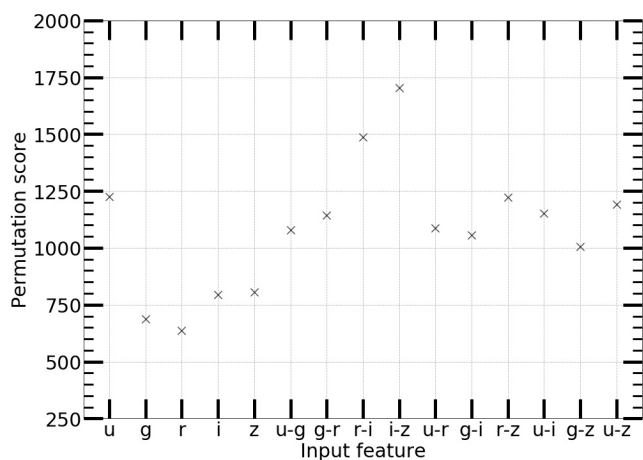


**Figure 22.** This figure shows the importance (N.B. a lower permutation score signifies greater importance) of each input feature to our background subtraction model, where the permutation score was based on the number of ‘actual’ cluster galaxies identified by our background subtraction model after randomly shuffling the data for each input feature.

utilised at all (i.e. if the galaxy was not randomly chosen to be in any of our training, validation or test sets), which is not maximising data efficiency. In future work, we could employ a k-fold cross-validation strategy (Bengio & Grandvalet 2004) for hyperparameter tuning and model evaluation. This would improve data efficiency and model generalisation as our background subtraction model would be evenly examined across all available data during its training and testing phases.

We performed permutation feature importance testing to determine which input features were deemed as important by our background subtraction model when identifying ‘actual’ cluster galaxies. From which, we found that the following input features displayed high significance:  $g$ ,  $r$ ,  $i$ ,  $z$ ,  $u-g$ ,  $u-r$ ,  $g-i$  and  $g-z$ . This tells us that our background subtraction model had learned to utilise most of the available photometric information in high dimensional colour-magnitude space. This was more efficient than only utilising a two dimensional colour-magnitude diagram, which is typically used when attempting to detect cluster galaxies within colour-magnitude space (e.g. Yee et al. 1999; Gladders & Yee 2005; Stott et al. 2009; Valentinuzzi et al. 2011). We believe that these specific input features were important to our background subtraction model due to two main reasons. Firstly, in Figure 14 it can be seen that the majority of the cluster and field galaxy population can be distinguished via filter magnitudes within colour-magnitude space.

This explained why our background subtraction model prioritised several filter magnitudes when performing background subtraction. Secondly, in Figure 14 it can also be seen that a minority of cluster galaxies overlapped with field galaxies within colour magnitude space. This explained why our background subtraction model also prioritised several colours in combination with the filter magnitudes to distinguish between these overlapping cluster and field galaxies. Based on these reasons, it is not unreasonable to assume that our background subtraction model can recognise the broad spectral features (e.g.  $4000\text{\AA}$  break) and overall shape of the observed spectral energy distribution<sup>21</sup> of cluster galaxies<sup>22</sup> at different redshifts.

In future work, it would be interesting to examine the impact from including additional features such as galaxy sizes, morphology and surface brightness as inputs for our background subtraction model. However, we note that we cannot easily reapply our method to galaxy surveys that do not readily provide information for all our required input features. Furthermore, our background subtraction model is not provided with redshift information as an input feature when distinguishing between cluster and field galaxies. Instead, we wanted our background subtraction model to self-learn about the photometric properties of cluster galaxies belonging to different redshift intervals, which is similar to how photometric redshifts of individual galaxies are estimated by empirical algorithms.

## 5 CONCLUSION

We present a proof-of-concept study of AutoEnRichness, a hybrid empirical and analytical approach that uses a multi-stage machine learning algorithm and a conventional luminosity distribution fitting approach to perform background subtraction and estimate cluster richnesses respectively. We utilised photometric data from the SDSS-IV DR16 to train our background subtraction model, which learned to reconstruct the photometry of cluster galaxies in order to distinguish between cluster and field galaxies. We then examined the predictive performance of our background subtraction model at distinguishing between cluster and field galaxies in a test set, which resulted in a balanced accuracy of 83.20 per cent. Subsequently, we constructed a scaling relation that estimated  $r_{200}$  when given the number of cluster galaxies identified by our background subtraction

<sup>21</sup> We recommend the reader to refer to Kennicutt (1992) for further details on the observed spectral energy distribution of different galaxies.

<sup>22</sup> Clusters typically have a majority population of elliptical and lenticular galaxies with a minority population of spiral galaxies (Dressler 1980).

model within a search radius of 2.5 Mpc at each cluster’s spectroscopic redshift. We utilised this learned scaling relation to resample galaxies within an  $r_{200}$  radius for each cluster. Next, we fitted the Schechter function to a composite luminosity distribution that consisted of a subsample of cluster galaxies identified by our background subtraction model within  $r_{200}$  that had high completeness. We used a Chi-squared fitting approach to determine an optimal  $r$  filter absolute magnitude bin size of 0.52 and best fit parameter values of  $M^* = -22.81$  with a standard deviation of  $\pm 0.5$ ;  $n^* = 159.82$  with a standard deviation of  $\pm 154.62$  and  $\alpha = -1.99$  with a standard deviation of  $\pm 0.37$ . We then used the optimal  $r$  filter absolute magnitude bin size and best fit parameter values for  $M^*$  and  $\alpha$  to fit the Schechter function to the luminosity distribution of individual clusters. We estimated cluster richnesses within  $r_{200}$  by computing the integral of the locally fit Schechter function. Lastly, we applied the optimal  $r$  filter absolute magnitude bin size and best fit parameter values for  $M^*$  and  $\alpha$  to another test set of clusters to obtain a median absolute percentage error of 33.50 per cent between our estimated cluster richnesses and WH15 richnesses within  $r_{200}$ . We note that the only cluster prerequisites for AutoEnRichness were the astronomical coordinates of the approximate cluster location as well as an initial cluster redshift estimate for computing appropriate cluster radii. We intend for AutoEnRichness to be combined with the Deep-CEE (Chan & Stott 2019) and Z-Sequence (Chan & Stott 2021) algorithms to obtain the key measurements (i.e. position from cluster detection and distance from redshift estimation respectively) needed for conducting astrophysics and cosmology research. In future work, it would be beneficial to develop a data pipeline that integrates AutoEnRichness with these other methods into an end-to-end process in preparation for usage on upcoming large-scale galaxy surveys, such as the Legacy Survey of Space and Time (Ivezic et al. 2019) and *Euclid* (Laureijs et al. 2011; Euclid Collaboration et al. 2019).

## ACKNOWLEDGEMENTS

We would like to thank the anonymous referee for their thorough feedback which has improved the clarity of our paper.

We gratefully acknowledge the support from the Science and Technologies Facilities Council studentship funding. We thank members of the XMM Cluster Survey for useful discussions. We would also like to thank the developers of VIZIER (Ochsenbein et al. 2000), TOPCAT (Taylor 2020), James Schombert at the University of Oregon, Edward L. Wright at the University of California, Los Angeles (Wright 2006), SCIKIT-LEARN (Pedregosa et al. 2011), SciPy (Virtanen et al. 2020) and TENSORFLOW (Abadi et al. 2015) for allowing the open distribution and free usage of their software for research.

Funding for the Sloan Digital Sky Survey IV has been provided by the Alfred P. Sloan Foundation, the U.S. Department of Energy Office of Science, and the Participating Institutions.

SDSS-IV acknowledges support and resources from the Center for High Performance Computing at the University of Utah. The SDSS website is [www.sdss.org](http://www.sdss.org).

SDSS-IV is managed by the Astrophysical Research Consortium for the Participating Institutions of the SDSS Collaboration including the Brazilian Participation Group, the Carnegie Institution for Science, Carnegie Mellon University, Center for Astrophysics | Harvard & Smithsonian, the Chilean Participation Group, the French Participation Group, Instituto de Astrofísica de Canarias, The Johns Hopkins University, Kavli Institute for the Physics and

Mathematics of the Universe (IPMU) / University of Tokyo, the Korean Participation Group, Lawrence Berkeley National Laboratory, Leibniz Institut für Astrophysik Potsdam (AIP), Max-Planck-Institut für Astronomie (MPIA Heidelberg), Max-Planck-Institut für Astrophysik (MPA Garching), Max-Planck-Institut für Extraterrestrische Physik (MPE), National Astronomical Observatories of China, New Mexico State University, New York University, University of Notre Dame, Observatório Nacional / MCTI, The Ohio State University, Pennsylvania State University, Shanghai Astronomical Observatory, United Kingdom Participation Group, Universidad Nacional Autónoma de México, University of Arizona, University of Colorado Boulder, University of Oxford, University of Portsmouth, University of Utah, University of Virginia, University of Washington, University of Wisconsin, Vanderbilt University, and Yale University.

## DATA AVAILABILITY

The AMF11 catalogue (Szabo et al. 2011) of individual cluster galaxies is publicly available on Vizier via: <http://vizier.u-strasbg.fr/viz-bin/VizieR-3?-source=J/ApJ/736/21/mg>. The SDSS-IV DR16 (Ahumada et al. 2020) photometry data of individual galaxies is also publicly available on Vizier via: <http://vizier.u-strasbg.fr/viz-bin/VizieR?-source=V/154>. Furthermore, the WH15 (Wen & Han 2015) and redMaPPer v6.3 (Rykoff et al. 2014) cluster catalogues can be found publicly via: <http://vizier.u-strasbg.fr/viz-bin/VizieR-3?-source=J/ApJ/807/178/table3> and <http://risa.stanford.edu/redmapper/>.

## REFERENCES

- Abadi M., et al., 2015, TensorFlow: Large-Scale Machine Learning on Heterogeneous Systems, <http://tensorflow.org/>
- Abell G. O., 1958, *ApJS*, 3, 211
- Abell G. O., 1975, Stars and Stellar Systems IX: Galaxies and the Universe, p. 601
- Adelman-McCarthy J. K., et al., 2008, *ApJS*, 175, 297
- Ahumada R., et al., 2020, *ApJS*, 249, 3
- Aihara H., et al., 2011, *ApJS*, 193, 29
- Alam S., et al., 2015, *ApJS*, 219, 12
- Alpaslan M., et al., 2012, *MNRAS*, 426, 2832
- Amodeo S., Ettori S., Capasso R., Sereno M., 2016, *A&A*, 590, A126
- Bahcall N. A., 1988, *ARA&A*, 26, 631
- Balland C., Blanchard A., 1995, arXiv e-prints, [pp astro-ph/9510130](https://arxiv.org/abs/ppastro-ph/9510130)
- Bengio Y., Grandvalet Y., 2004, The Journal of Machine Learning Research, 5, 1089
- Bergstra J., Bengio Y., 2012, The Journal of Machine Learning Research, 13, 281
- Biviano A., Girardi M., 2003, *ApJ*, 585, 205
- Boué G., Adami C., Durret F., Mamon G. A., Cayatte V., 2008, *A&A*, 479, 335
- Boyd K., Eng K. H., Page C. D., 2013, in Proceedings of the 2013th European Conference on Machine Learning and Knowledge Discovery in Databases - Volume Part III. ECMLPKDD’13. Springer-Verlag, Berlin, Heidelberg, pp 451–466, [doi:10.1007/978-3-642-40994-3\\_29](https://doi.org/10.1007/978-3-642-40994-3_29), [https://doi.org/10.1007/978-3-642-40994-3\\_29](https://doi.org/10.1007/978-3-642-40994-3_29)
- Breiman L., 2001, Machine Learning, 45, 5
- Brodersen K. H., Ong C. S., Stephan K. E., Buhmann J. M., 2010, in 2010 20th International Conference on Pattern Recognition. pp 3121–3124, [doi:10.1109/ICPR.2010.764](https://doi.org/10.1109/ICPR.2010.764)
- Bruzual G., Charlot S., 2003, *MNRAS*, 344, 1000



- Calvi R., Poggianti B. M., Vulcani B., 2011, *MNRAS*, **416**, 727
- Carlberg R. G., Yee H. K. C., Ellingson E., 1997, *ApJ*, **478**, 462
- Carlberg R. G., Yee H. K. C., Morris S. L., Lin H., Hall P. B., Patton D., Sawicki M., Shepherd C. W., 2000, *ApJ*, **542**, 57
- Carlstrom J. E., Holder G. P., Reese E. D., 2002, *ARA&A*, **40**, 643
- Castander F. J., et al., 1995, *Nature*, **377**, 39
- Castro T., Marra V., Quartin M., 2016, *MNRAS*, **463**, 1666
- Chan M. C., Stott J. P., 2019, *MNRAS*, **490**, 5770
- Chan M. C., Stott J. P., 2021, *MNRAS*, **503**, 6078
- Chen T., Guestrin C., 2016, in Proceedings of the 22nd ACM SIGKDD International Conference on Knowledge Discovery and Data Mining. KDD '16. Association for Computing Machinery, New York, NY, USA, pp 785–794, doi:10.1145/2939672.2939785, https://doi.org/10.1145/2939672.2939785
- Chollet F., et al., 2015, *Keras*, https://keras.io
- Cohn J. D., Battaglia N., 2019, *MNRAS*, **491**, 1575
- Cohn J. D., White M., 2005, *Astroparticle Physics*, **24**, 316
- Cortes C., Vapnik V., 2009, *Chem. Biol. Drug Des.*, **297**, 273
- Costanzi M., et al., 2018, *MNRAS*, **482**, 490
- Csabai I., Dobos L., Trencsényi M., Herczegh G., Józsa P., Purger N., Budavári T., Szalay A. S., 2007, *Astronomische Nachrichten*, **328**, 852
- Dannerbauer H., et al., 2019, *BAAS*, **51**, 293
- Davis M., Huchra J., Latham D. W., Tonry J., 1982, *ApJ*, **253**, 423
- Davis M., Efstathiou G., Frenk C. S., White S. D. M., 1985, *ApJ*, **292**, 371
- Diaferio A., Geller M. J., 1997, *ApJ*, **481**, 633
- Diaferio A., Geller M. J., Rines K. J., 2005, *ApJ*, **628**, L97
- Dong F., Pierpaoli E., Gunn J. E., Wechsler R. H., 2008, *ApJ*, **676**, 868
- Dressler A., 1980, *ApJ*, **236**, 351
- Ebeling H., Edge A. C., Mantz A., Barrett E., Henry J. P., Ma C. J., van Speybroeck L., 2010, *MNRAS*, **407**, 83
- Ettori S., Donnarumma A., Pointecouteau E., Reiprich T. H., Giodini S., Lovisari L., Schmidt R. W., 2013, *Space Sci. Rev.*, **177**, 119
- Euclid Collaboration et al., 2019, *A&A*, **627**, A23
- Farrens S., Abdalla F. B., Cypriano E. S., Sabiu C., Blake C., 2011, *MNRAS*, **417**, 1402
- Fix E., 1951, Technical report, Discriminatory analysis: nonparametric discrimination, consistency properties. Randolph Field, Texas, USA
- Frenk C. S., White S. D. M., Efstathiou G., Davis M., 1990, *ApJ*, **351**, 10
- Geller M. J., Diaferio A., Kurtz M. J., 1999, *ApJ*, **517**, L23
- Gladders M. D., Yee H. K. C., 2005, *ApJS*, **157**, 1
- Glorot X., Bengio Y., 2010, in Teh Y. W., Titterton M., eds, Proceedings of Machine Learning Research Vol. 9, Proceedings of the Thirteenth International Conference on Artificial Intelligence and Statistics. PMLR, Chia Laguna Resort, Sardinia, Italy, pp 249–256, https://proceedings.mlr.press/v9/glorot10a.html
- Goto T., et al., 2003, *PASJ*, **55**, 739
- Gupta N., Reichardt C. L., 2020, *ApJ*, **900**, 110
- Hansen S. M., McKay T. A., Wechsler R. H., Annis J., Sheldon E. S., Kimball A., 2005, *ApJ*, **633**, 122
- He K., Zhang X., Ren S., Sun J., 2015, in 2015 IEEE International Conference on Computer Vision (ICCV). pp 1026–1034, doi:10.1109/ICCV.2015.123
- Ho M., Rau M. M., Ntampaka M., Farahi A., Trac H., Póczos B., 2019, *ApJ*, **887**, 25
- Hoekstra H., Bartelmann M., Dahle H., Israel H., Limousin M., Meneghetti M., 2013, *Space Sci. Rev.*, **177**, 75
- Huchra J. P., Geller M. J., 1982, *ApJ*, **257**, 423
- Huss A., Jain B., Steinmetz M., 1999, *MNRAS*, **308**, 1011
- Ivezić Ž., et al., 2019, *ApJ*, **873**, 111
- Johnston D. E., Sheldon E. S., Tasitsiomi A., Frieman J. A., Wechsler R. H., McKay T. A., 2007, *ApJ*, **656**, 27
- Kennicutt Robert C. J., 1992, *ApJS*, **79**, 255
- Kepner J., Fan X., Bahcall N., Gunn J., Lupton R., Xu G., 1999, *ApJ*, **517**, 78
- Kingma D. P., Welling M., 2013, arXiv e-prints, p. arXiv:1312.6114
- Kneißl R., Jones M. E., Saunders R., Eke V. R., Lasenby A. N., Grainge K., Cotter G., 2001, *MNRAS*, **328**, 783
- Kodama T., Smail I., Nakata F., Okamura S., Bower R. G., 2001, *ApJ*, **562**, L9
- Koester B. P., et al., 2007, *ApJ*, **660**, 221
- Kravtsov A. V., Borgani S., 2012, *ARA&A*, **50**, 353
- Laureijs R., et al., 2011, arXiv e-prints, p. arXiv:1110.3193
- Liang H., Sun X., Yunlei S., Gao Y., 2017, *EURASIP Journal on Wireless Communications and Networking*, 2017
- Lin S.-C., Su Y., Liang G., Zhang Y., Jacobs N., Zhang Y., 2022, *MNRAS*, **512**, 3885
- Lipton Z. C., Elkan C., Narayanaswamy B., 2014, arXiv preprint arXiv:1402.1892
- Liu F. T., Ting K. M., Zhou Z.-H., 2008, in 2008 Eighth IEEE International Conference on Data Mining. pp 413–422, doi:10.1109/ICDM.2008.17
- Liu Q., Zhang J., Liu J., Yang Z., 2022, *International Journal of Machine Learning and Cybernetics*, **13**, 1685
- Macqueen J., 1967, in In 5-th Berkeley Symposium on Mathematical Statistics and Probability. University of California Press, Oakland, California, USA, pp 281–297
- McClintock T., et al., 2019, *MNRAS*, **482**, 1352
- Melin J. B., Bartlett J. G., Delabrouille J., 2005, *A&A*, **429**, 417
- Morgan S. P., Teachman J. D., 1988, *Journal of Marriage and Family*, **50**, 929
- Nair V., Hinton G. E., 2010, in Proceedings of the 27th International Conference on International Conference on Machine Learning. ICMML 10. Omnipress, Madison, WI, USA, pp 807–814
- Notley S., Magdon-Ismael M., 2018, arXiv e-prints, p. arXiv:1805.02294
- Ntampaka M., et al., 2019, *ApJ*, **876**, 82
- O' Mahony N., Campbell S., Carvalho A., Harapanahalli S., Velasco-Hernandez G., Krpalkova L., Riordan D., Walsh J., 2019, arXiv e-prints, p. arXiv:1910.13796
- Ochsenbein F., Bauer P., Marcout J., 2000, *A&AS*, **143**, 23
- Oegerle W. R., Hoessel J. G., 1989, *AJ*, **98**, 1523
- Oegerle W. R., Hoessel J. G., Jewison M. S., 1987, *AJ*, **93**, 519
- Owers M. S., et al., 2017, *MNRAS*, **468**, 1824
- Paolillo M., Andreon S., Longo G., Puddu E., Gal R. R., Scaramella R., Djorgovski S. G., de Carvalho R., 2001, *A&A*, **367**, 59
- Pedregosa F., et al., 2011, *The Journal of Machine Learning Research*, **12**, 2825
- Planck Collaboration et al., 2014, *A&A*, **571**, A17
- Pointecouteau E., Arnaud M., Pratt G. W., 2005, *A&A*, **435**, 1
- Popesso P., Böhringer H., Brinkmann J., Voges W., York D. G., 2004, *A&A*, **423**, 449
- Popesso P., Böhringer H., Romaniello M., Voges W., 2005, *A&A*, **433**, A15
- Postman M., Lubin L. M., Gunn J. E., Oke J. B., Hoessel J. G., Schneider D. P., Christensen J. A., 1996, *AJ*, **111**, 615
- Rauzy S., Adami C., Mazure A., 1998, *A&A*, **337**, 31
- Reblinsky K., Bartelmann M., 1999, *A&A*, **345**, 1
- Refregier A., 2003, *ARA&A*, **41**, 645
- Rines K., Geller M. J., Diaferio A., Kurtz M. J., 2013, *ApJ*, **767**, 15
- Rodríguez F., Merchán M., 2020, *A&A*, **636**, A61
- Ruder S., 2016, arXiv e-prints, p. arXiv:1609.04747
- Rumelhart D., Hinton G., Williams R., 1985, *Learning Internal Representations by Error Propagation*. Institute for Cognitive Science, University of California, San Diego
- Rykoff E. S., et al., 2014, *ApJ*, **785**, 104
- Sanderson A. J. R., Ponman T. J., 2010, *MNRAS*, **402**, 65
- Sarazin C. L., 1986, *Reviews of Modern Physics*, **58**, 1
- Schechter P., 1976, *ApJ*, **203**, 297
- Schlafly E. F., Finkbeiner D. P., 2011, *ApJ*, **737**, 103
- Schlegel D. J., Finkbeiner D. P., Davis M., 1998, *ApJ*, **500**, 525
- Stott J. P., Smail I., Edge A. C., Ebeling H., Smith G. P., Kneib J.-P., Pimblett K. A., 2007, *ApJ*, **661**, 95
- Stott J. P., Pimblett K. A., Edge A. C., Smith G. P., Wardlow J. L., 2009, *MNRAS*, **394**, 2098
- Strazzullo V., et al., 2019, *A&A*, **622**, A117
- Sunayama T., et al., 2020, *MNRAS*, **496**, 4468
- Szabo T., Pierpaoli E., Dong F., Pipino A., Gunn J., 2011, *ApJ*, **736**, 21
- Taylor M. B., 2020, in Ballester P., Ibsen J., Solar M., Shorridge K., eds,



- Astronomical Society of the Pacific Conference Series Vol. 522, Astronomical Data Analysis Software and Systems XXVII. p. 67
- Tempel E., Kipper R., Tamm A., Gramann M., Einasto M., Sepp T., Tuvikene T., 2016, *A&A*, 588, A14
- Tsai J. C., Buote D. A., 1996, *MNRAS*, 282, 77
- Umetsu K., Broadhurst T., Zitrin A., Medezinski E., Coe D., Postman M., 2011, *ApJ*, 738, 41
- Valentinuzzi T., et al., 2011, *A&A*, 536, A34
- Valotto C. A., Nicotra M. A., Muriel H., Lambas D. G., 1997, *ApJ*, 479, 90
- Van Waerbeke L., et al., 2013, *MNRAS*, 433, 3373
- Virtanen P., et al., 2020, *Nature Methods*, 17, 261
- Voigt L. M., Fabian A. C., 2006, *MNRAS*, 368, 518
- Weinberg D. H., 2005, *Science*, 309, 564
- Wen Z. L., Han J. L., 2015, *ApJ*, 807, 178
- Wen Z. L., Han J. L., Liu F. S., 2009, *ApJS*, 183, 197
- Wen Z. L., Han J. L., Liu F. S., 2012, *ApJS*, 199, 34
- Wilson G., 2003, *ApJ*, 585, 191
- Wright E. L., 2006, *PASP*, 118, 1711
- Wylezalek D., et al., 2014, *ApJ*, 786, 17
- Yan Z., Mead A., Van Waerbeke L., Hinshaw G., McCarthy I., 2020, *MNRAS*, 499, 3445
- Yang X., Mo H. J., van den Bosch F. C., Jing Y. P., 2005, *MNRAS*, 356, 1293
- Yee H. K. C., Gladders M. D., López-Cruz O., 1999, in Weymann R., Storrie-Lombardi L., Sawicki M., Brunner R., eds, *Astronomical Society of the Pacific Conference Series Vol. 191, Photometric Redshifts and the Detection of High Redshift Galaxies*. p. 166 ([arXiv:astro-ph/9908001](https://arxiv.org/abs/astro-ph/9908001))
- Yennapureddy M. K., Melia F., 2019, *European Physical Journal C*, 79, 571
- Zhao Y., Nasrullah Z., Li Z., 2019, *The Journal of Machine Learning Research*, 20, 1
- Zwicky F., 1957, *Morphological Astronomy*. Springer Verlag
- Zwicky F., Herzog E., Wild P., Karpowicz M., Kowal C. T., 1961, *Catalogue of galaxies and of clusters of galaxies, Vol. I*. California Institute of Technology, Pasadena, California, USA
- de Andres D., et al., 2022, in *EPJ Web of Conferences*. p. 00013
- de Lapparent V., 1994, in MacGillivray H. T., ed., *Vol. 161, Astronomy from Wide-Field Imaging*. p. 669
- van Haarlem M. P., 1996, in Coles P., Martinez V., Pons-Borderia M.-J., eds, *Astronomical Society of the Pacific Conference Series Vol. 94, Mapping, Measuring, and Modelling the Universe*. p. 191 ([arXiv:astro-ph/9601081](https://arxiv.org/abs/astro-ph/9601081))
- van Haarlem M. P., Frenk C. S., White S. D. M., 1997, *MNRAS*, 287, 817
- van Uitert E., Gilbank D. G., Hoekstra H., Semboloni E., Gladders M. D., Yee H. K. C., 2016, *A&A*, 586, A43

**Supplementary material (online)**

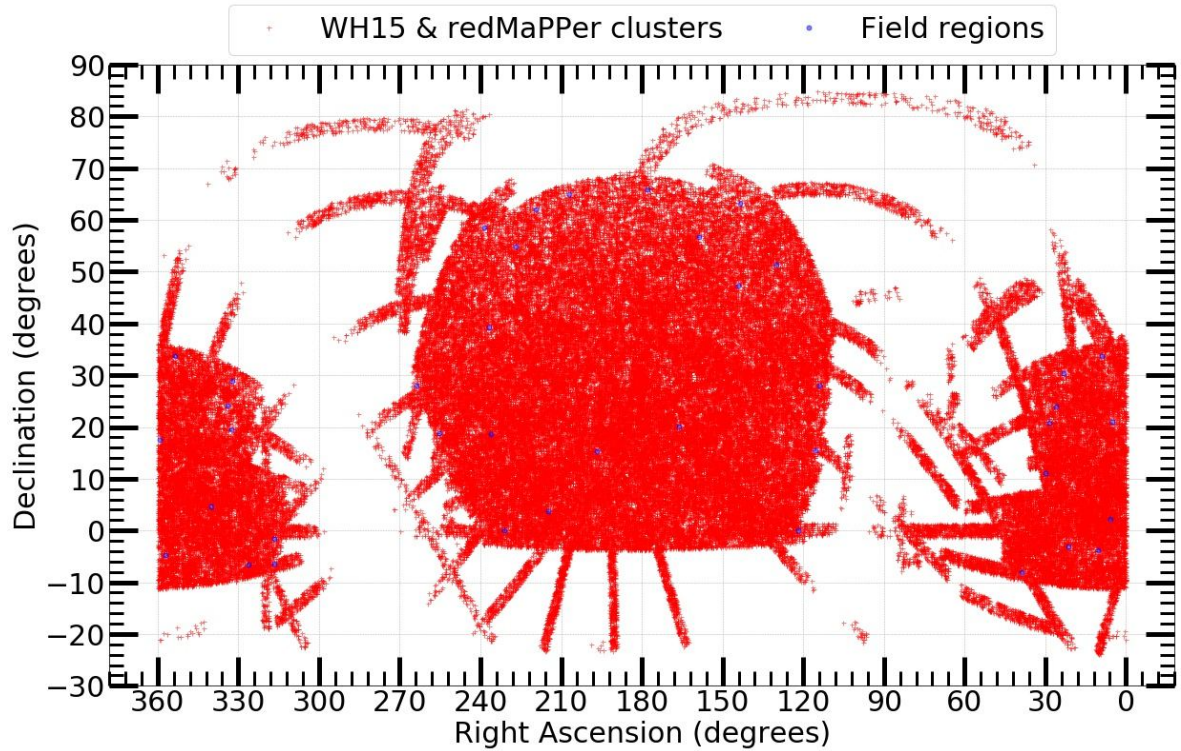


**Figure S1.** This figure displays a sky map of the astronomical coordinates (J2000) for the WH15 and redMaPPer clusters (red cross) as well as the astronomical coordinates of our forty different proposed ‘field’ regions (blue circle).

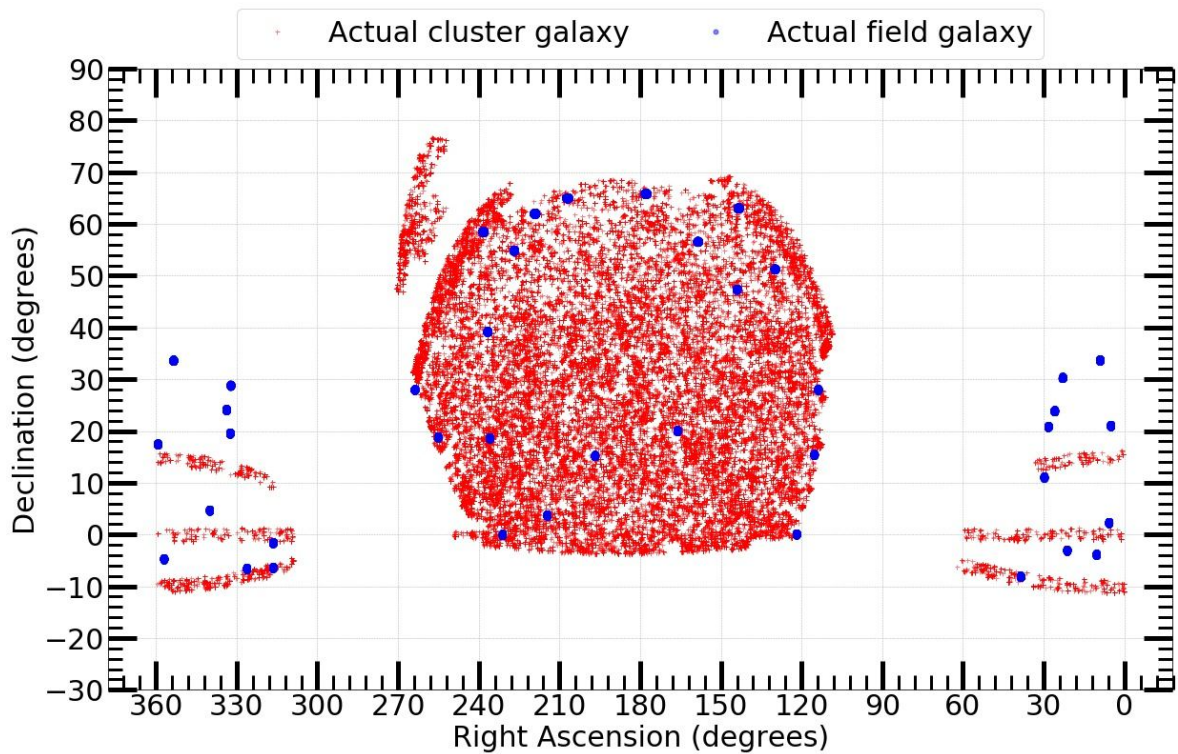


**Figure S2.** This figure displays a sky map of the astronomical coordinates (J2000) for the cluster (red cross) and field (blue circle) galaxies that had been cross-matched with galaxies observed within SDSS-IV DR16.

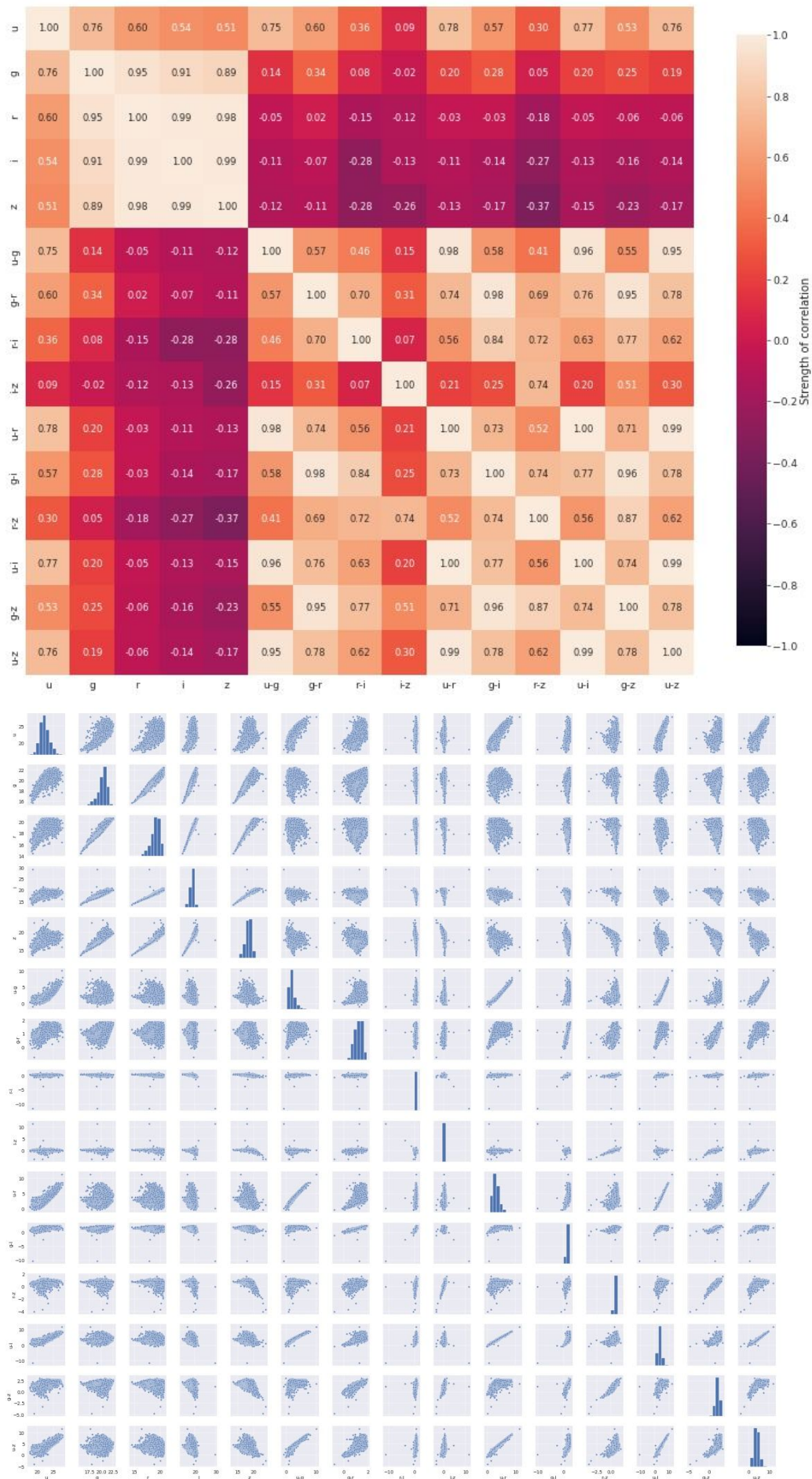


**Figure S3.** This figure displays a correlation matrix heatmap (top image) and scatterplots (bottom image) of features (i.e. filters and colours) from optical photometry data of galaxies in our cluster galaxy sample. The colourbar for the correlation matrix heatmap represents the strength and direction of the linear correlation between features.



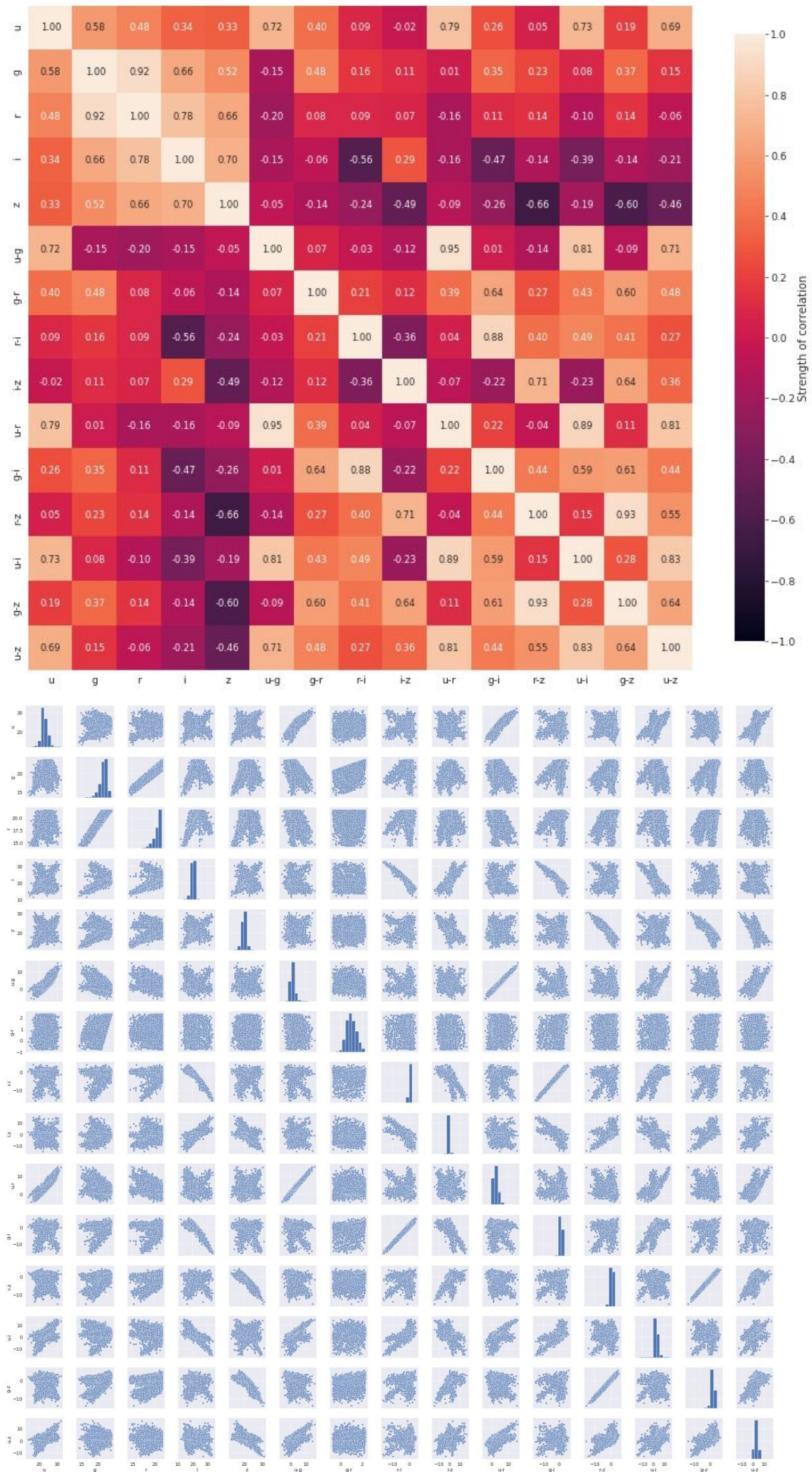


**Figure S4.** This figure is the same as Figure S3 except it is showing galaxies in our field galaxy sample.

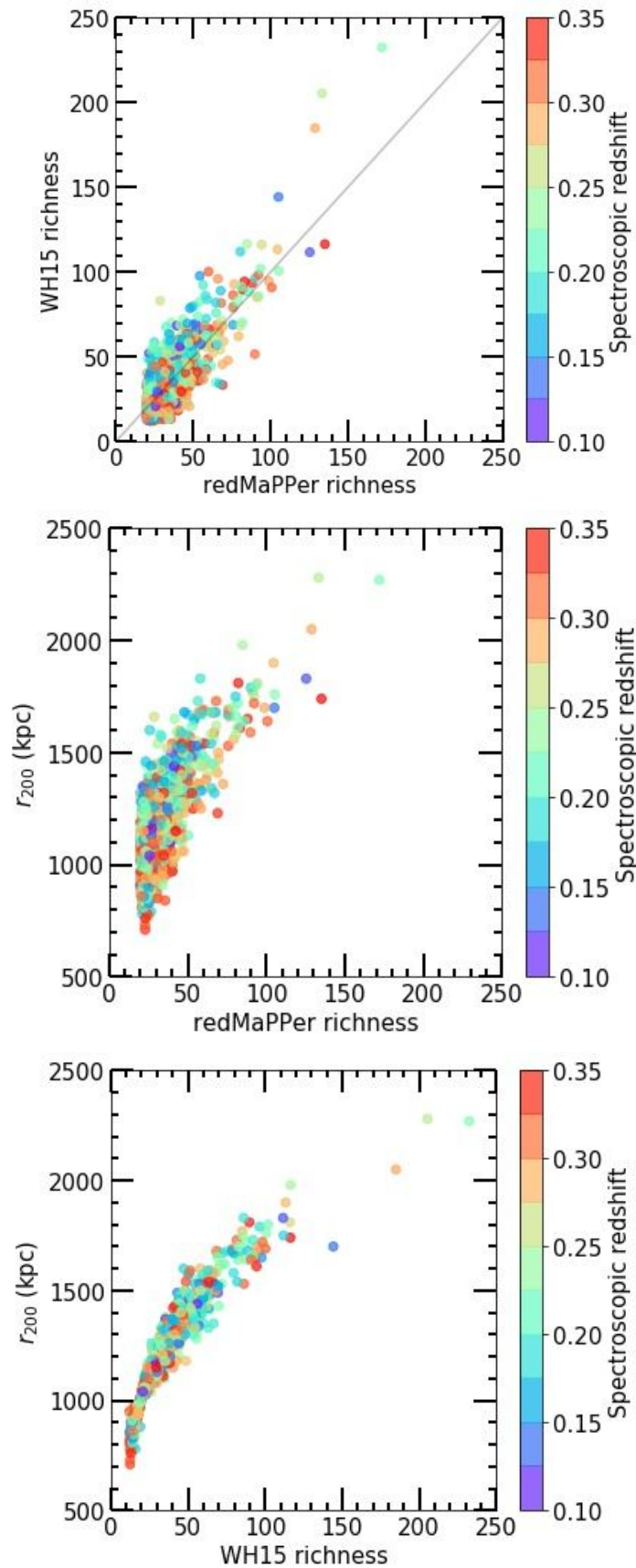


**Figure S5.** Top image: this figure displays a direct comparison between redMaPPer and WH15 richness for a subsample of cross-matched WH15 and redMaPPer clusters between a redshift range of  $0.1 \leq z \leq 0.35$ . Middle image: this figure displays a direct comparison between redMaPPer richness and  $r_{200}$  values determined by WH15 for a subsample of cross-matched WH15 and redMaPPer clusters between a redshift range of  $0.1 \leq z \leq 0.35$ . Bottom image: this figure displays a direct comparison between WH15 richness and  $r_{200}$  values determined by WH15 for a subsample of cross-matched WH15 and redMaPPer clusters between a redshift range of  $0.1 \leq z \leq 0.35$ .

Random search iteration	Batch size	Learning rate	Optimiser algorithm	Architecture layout	AUCPR (per cent) [mean]	AUCPR (per cent) [standard deviation]
1	512	0.0001	'RMSprop'	5	39.87	1.52
2	2048	0.01	'Adadelata'	1	34.03	2.46
3	2048	0.001	'Adam'	5	38.93	1.27
4	1024	0.1	'Adadelata'	5	38.94	2.14
5	512	0.001	'SGD'	5	38.41	3.71
6	2048	0.0001	'Adagrad'	3	33.68	1.22
7	256	0.001	'Adam'	1	39.95	1.41
8	2048	0.0001	'Adadelata'	1	34.02	0.35
9	256	0.1	'Adadelata'	1	37.74	2.95
10	256	0.0001	'Adadelata'	1	34.15	0.37
11	1024	0.001	'Adadelata'	1	35.29	1.97
12	1024	0.0001	'Nadam'	1	39.28	2.05
13	512	0.0001	'RMSprop'	1	38.93	2.38
14	256	0.1	'Adadelata'	5	39.18	1.30
15	1024	0.0001	'Nadam'	5	39.23	2.36
16	256	0.01	'Adagrad'	1	39.17	2.47
17	512	0.0001	'Nadam'	3	38.65	1.63
18	512	0.1	'Nadam'	1	34.08	0.34
19	1024	0.1	'Adam'	3	35.82	3.34
20	2048	0.1	'SGD'	5	38.48	1.51
21	1024	0.01	'Adagrad'	3	39.00	3.01
22	256	0.1	'Nadam'	5	34.08	0.34
23	1024	0.1	'Adamax'	5	37.88	3.12
24	1024	0.0001	'Adadelata'	3	33.74	0.98
25	2048	0.001	'RMSprop'	1	39.50	2.07
26	1024	0.01	'Nadam'	1	38.99	2.12
27	256	0.01	'Adadelata'	3	38.89	1.69
28	512	0.001	'Nadam'	3	39.51	1.43
29	512	0.01	'Adagrad'	1	38.52	3.34
30	256	0.0001	'Adamax'	3	38.05	1.25
31	512	0.001	'SGD'	3	38.20	1.90
32	1024	0.1	'Adagrad'	5	37.83	2.89
33	512	0.01	'Adamax'	1	38.51	2.72
34	1024	0.01	'Adam'	3	37.15	2.08
35	256	0.001	'Adagrad'	1	36.44	2.80
36	1024	0.1	'Adadelata'	3	38.08	2.24
37	2048	0.001	'Adadelata'	1	33.83	2.25
38	256	0.1	'Adam'	1	34.08	0.34
39	1024	0.0001	'Adagrad'	5	34.09	1.48
40	512	0.01	'Adadelata'	1	37.93	2.83
41	1024	0.0001	'Adamax'	5	40.03	1.24
42	2048	0.0001	'Adam'	5	39.26	2.00
43	256	0.01	'Nadam'	5	39.15	2.27
44	2048	0.0001	'RMSprop'	3	40.24	1.85
45	1024	0.1	'Nadam'	5	34.08	0.34
46	512	0.0001	'Adam'	5	37.64	2.09
47	2048	0.001	'Nadam'	1	39.38	2.45
48	1024	0.1	'Nadam'	3	34.08	0.34
49	512	0.1	'Adadelata'	3	39.29	1.38
50	1024	0.0001	'RMSprop'	1	39.36	2.19
51	2048	0.0001	'RMSprop'	1	38.92	2.20
52	256	0.0001	'Adagrad'	1	34.73	1.61
53	256	0.001	'SGD'	1	37.09	2.16
54	1024	0.01	'RMSprop'	1	37.56	3.23
55	512	0.001	'Adamax'	5	38.17	2.19
56	1024	0.0001	'SGD'	3	33.55	2.83
57	512	0.01	'SGD'	5	38.79	2.05
58	1024	0.001	'SGD'	1	34.61	3.00
59	1024	0.01	'Adadelata'	5	37.68	1.74
60	256	0.01	'RMSprop'	5	38.93	1.80

**Table S1.** This table displays the randomly selected hyper-parameter (i.e. batch size, learning rate, optimiser algorithm and architecture layout) combinations for tuning our background subtraction model on galaxies in our validation set using sixty iterations of random search. We also display the mean and standard deviation of the resultant AUCPR from performing ten iterations of Monte Carlo cross-validation on each random search iteration.



Class probability threshold	F1 score (per cent)
0	40.00
0.01	42.43
0.02	42.66
0.03	42.81
0.04	42.96
0.05	43.07
0.06	43.26
0.07	43.38
0.08	43.49
0.09	43.59
0.1	43.67
0.11	43.76
0.12	43.87
0.13	44.03
0.14	44.19
0.15	44.36
0.16	44.54
0.17	44.77
0.18	44.97
0.19	45.15
0.2	45.32
0.21	45.62
0.22	45.99
0.23	46.32
0.24	46.83
0.25	47.47
0.26	47.96
0.27	48.31
0.28	48.69
0.29	48.92
0.3	48.69
0.31	45.18
0.32	19.17
0.33	0.00
0.34	0.00
0.35	0.00
0.36	0.00
0.37	0.00
0.38	0.00
0.39	0.00
0.4	0.00
0.41	0.00
0.42	0.00
0.43	0.00
0.44	0.00
0.45	0.00
0.46	0.00
0.47	0.00
0.48	0.00
0.49	0.00
0.5	0.00
0.51	0.00
0.52	0.00
0.53	0.00
0.54	0.00
0.55	0.00
0.56	0.00
0.57	0.00
0.58	0.00
0.59	0.00
0.6	0.00
0.61	0.00
0.62	0.00
0.63	0.00
0.64	0.00
0.65	0.00
0.66	0.00
0.67	0.00
0.68	0.00
0.69	0.00
0.7	0.00
0.71	0.00
0.72	0.00
0.73	0.00
0.74	0.00
0.75	0.00
0.76	0.00
0.77	0.00
0.78	0.00
0.79	0.00
0.8	0.00
0.81	0.00
0.82	0.00
0.83	0.00
0.84	0.00
0.85	0.00
0.86	0.00
0.87	0.00
0.88	0.00
0.89	0.00
0.9	0.00
0.91	0.00
0.92	0.00
0.93	0.00
0.94	0.00
0.95	0.00
0.96	0.00
0.97	0.00
0.98	0.00
0.99	0.00
1	0.00

**Table S2.** This table displays the resultant F1 scores on galaxies in our validation set when using different class probability thresholds with the optimal hyper-parameter combination for our background subtraction model. It should be noted that an F1 score of 0 signifies that no cluster galaxies were identified at the given class probability threshold.

Bin size	Chi-square fitting error	Number of bins with galaxies	$M^*$	$M^*$ [standard deviation]	$n^*$	$n^*$ [standard deviation]	$\alpha$	$\alpha$ [standard deviation]
0.01	102.140920976604	147	-25.3072697006017	7.28783936301292	0.164112608931114	1.38199927866705	-2	0.466629082092991
0.02	76.5453069917579	87	-22.8960081024292	1.09379460105731	4.71921420366664	9.20338546553196	-2	0.580632607165434
0.03	68.1745019597015	65	-22.4908977078703	0.790075482406013	12.70439476778	18.952684149263	-1.99999999999989	0.599104919143905
0.04	61.266861269483	50	-22.415789304908	0.756339770593328	19.3568690083877	27.8274793059772	-1.99999999999979	0.608973124211291
0.05	39.6185650543927	43	-22.6222052707545	0.672513724488882	18.3176186296316	23.2838977629391	-1.99999999999999	0.486524958545581
0.06	36.5625019331505	37	-22.6258973735442	0.626947096373978	21.9653980090031	26.0819814894214	-1.99999999999946	0.458571758087398
0.07	33.5900501761644	33	-22.6099206948986	0.602242351450481	26.3737283301809	30.2193978963726	-1.99999999999887	0.451033803392379
0.08	29.6385878283548	28	-22.5816910642751	0.591756403834509	31.7971766662677	35.8707702408829	-1.99999999999999	0.452169800589196
0.09	20.3637951180156	27	-22.6746874027806	0.521101827729886	31.5718547496863	31.5686519817016	-1.99999999999869	0.393056307595776
0.1	16.5530148685729	23	-22.6582443109673	0.569061669900563	36.3423806202571	39.4465302657616	-1.99999999999955	0.421022202247245
0.11	13.0767631976711	21	-22.6755620489245	0.5251309291653	39.2543259599577	41.4152567582025	-1.99999999999977	0.408316979552766
0.12	15.2459769970052	19	-22.7247184161576	0.591396789212753	39.7619946638302	44.3787960605664	-2	0.411200351509468
0.13	9.14827055635872	19	-22.6183758110969	0.458502287321535	52.1384807705458	45.3748880546628	-1.95453486711378	0.371591371552821
0.14	11.7492730266906	18	-22.643331608495	0.462615820139636	52.7951370756613	47.0457807096035	-1.98924101376669	0.367764744434002
0.15	10.9037429665667	16	-22.4923685847581	0.448002369078026	74.7956455459639	61.8368875874148	-1.88377867043106	0.397289759070223
0.16	16.772278347289	15	-22.5384337422092	0.475641293653476	70.5894407833445	64.5502898072399	-1.97587961393189	0.404297179863603
0.17	4.15402355091424	15	-22.7292157905515	0.466124335935932	56.9967978748963	51.1443097694934	-2	0.351042953646424
0.18	12.7790690539623	14	-22.6591309218703	0.490607883863879	65.8069565315428	62.2084888857685	-1.99999999999884	0.381498515390209
0.19	10.1521887967407	13	-22.7126392343591	0.531049352235773	64.521848195881	65.4523309529134	-2	0.389521040297862
0.2	7.99147466406507	12	-22.7208482829558	0.537766203637089	67.4775596294566	69.1927939236387	-2	0.39096836606222
0.21	4.29404454893266	12	-22.7778047368944	0.507161177536059	65.6184421027745	63.563335472533	-2	0.363579536524285
0.22	5.67230887264036	11	-22.7623890236569	0.525989016830309	70.1952555544012	70.3336011457905	-2	0.374685241450145
0.23	3.92256129130857	11	-22.705216487009	0.489026439161547	80.1076053301875	75.3087082850019	-2	0.369199150776928
0.24	8.17416297511997	10	-22.5708243936802	0.46728589789064	104.425526335234	92.3190354948186	-1.94542652350871	0.390175180596096
0.25	4.29832445617372	10	-22.7749629261976	0.504034834908083	78.5599805972613	75.5810214476751	-1.99999999999975	0.360888114340128
0.26	1.5900013241842	10	-22.7543979409332	0.456121860305321	84.6673328318602	74.3374090694452	-2	0.340403198275327
0.27	4.97043601393654	9	-22.732623940767	0.537509637953644	90.2958645221638	92.7197761899969	-2	0.390545267175811
0.28	4.10694483459387	9	-22.7361583932848	0.475351264466895	94.4841506940494	85.5761639766845	-1.97909263203428	0.35665435560158
0.29	2.43440108474398	9	-22.7735764454752	0.483748588363934	91.7522170908038	85.1097978159416	-2	0.353263598483103
0.3	5.15205257540707	8	-22.7918350993829	0.571519770757192	92.0936083899066	99.5684604796216	-2	0.393299649494388
0.31	5.90218198017966	8	-22.7496055699693	0.512441830655374	101.027295842528	99.0607465472664	-1.99999999999849	0.374980540977817
0.32	10.1014409330581	8	-22.7068155761029	0.46673483659344	110.104060272333	99.3073073638942	-2	0.361982802750744
0.33	9.96846341699309	8	-22.7291063048754	0.46925404584864	109.201691285243	98.8710176390871	-2	0.356791209942564
0.34	1.12105000461229	8	-22.7478245333539	0.440292188347238	112.250370963957	95.4874446889144	-2	0.336758675291583
0.35	3.12523238008784	7	-22.782228568726	0.546318661436639	109.623965612747	113.882723095951	-1.99999999999999	0.387523819700969
0.36	3.03061687353762	7	-22.7241788039726	0.52765200413997	122.841382114879	123.931590655044	-2	0.390545298402819
0.37	1.48984677624025	7	-22.7309176072148	0.46076140879309	125.422731293451	111.639466908686	-2	0.354493289723339
0.38	2.36115567803497	7	-22.758776999429	0.469319697928797	123.406631037008	111.329064686043	-2	0.350817563549449
0.39	0.603516773400222	7	-22.6964112181343	0.413245262968147	140.371839664555	112.444496886239	-1.98962179171752	0.334505631972704
0.4	0.637438766276678	6	-22.7621355562676	0.547164384340818	130.14248212713	135.853063636089	-2	0.394672140845081
0.41	1.03851432178477	6	-22.7388960765666	0.539100941022473	137.925294842631	142.459296913682	-1.99999999999998	0.398317582214352
0.42	0.617019282021179	6	-22.7836403833345	0.52063968702413	132.412600884289	131.908715973817	-2	0.377789372068514
0.43	1.0022006125957	6	-22.7669424142399	0.497083941926808	138.844175703839	132.560878756468	-2	0.368534172557065
0.44	1.3854524348229	6	-22.735461750642	0.442508674389626	149.866239382466	127.730806309675	-1.98775443119698	0.344888791011023
0.45	2.09325476913197	6	-22.7542533806967	0.455514311827121	147.815629869087	129.964796940122	-2	0.347242980067736
0.46	2.06708478166107	6	-22.7198920761451	0.449235034517127	159.112883886869	138.59783627731	-2	0.353667237181105
0.47	1.91277317747975	6	-22.7134175644432	0.4158846753342	164.305815020088	133.021223122312	-1.99999999999996	0.33502131248639
0.48	3.09959702941975	5	-22.7133128234714	0.526534407663765	168.666330230149	170.028242094597	-1.991839331825	0.400161540375978
0.49	2.99396275206369	5	-22.7586216420838	0.530865270015062	160.296570599804	163.000668703465	-1.99999999999998	0.391406599797717
0.5	3.01068130899773	5	-22.7996514653902	0.532221118709986	154.04407380113	156.784199434023	-1.99999999999812	0.383433470402977
0.51	1.10735348985882	5	-22.8207986936304	0.529542207845286	153.028828033463	154.869239126894	-1.99999999999999	0.37851641868231
0.52	0.566621255611028	5	-22.8082232056862	0.504804314046596	159.821770266413	154.624246072466	-1.99360356962263	0.370844073513688
0.53	0.804364552288225	5	-22.5216510211879	0.418951220094654	274.838166240616	202.702584893226	-1.77308302024065	0.391484698263154
0.54	2.39612065033725	5	-22.5437634518665	0.441778546861592	265.78170850412	210.927359077781	-1.8183753728052	0.401173098435923
0.55	1.46317886420762	5	-22.4701482130265	0.382373057404958	310.083447783411	206.11140981392	-1.74205611806367	0.377492189289949
0.56	1.51574912980039	5	-22.5086962590682	0.3905000766944	297.455379636805	203.562572401559	-1.75836724883236	0.375135903611389
0.57	1.45663254988623	5	-22.5602264810274	0.402236411508689	278.002178944076	199.230027703658	-1.79306653623351	0.372083907644912
0.58	0.719369820743466	5	-22.6910262019285	0.426822999134624	223.608144930381	178.401952889802	-1.90202692521294	0.3585602913609
0.59	0.589469793678187	5	-22.603110886294	0.376524243377872	267.158181157209	183.285827177277	-1.83213557762778	0.345949650208558

**Table S3.** This table displays the computed Chi-square fitting errors when fitting the Schechter function to a composite luminosity distribution that consisted of a subsample of identified cluster galaxies from our CMWR- $r_{200}$  training set that visually appeared to have high completeness. We also display the best fit parameter values for  $M^*$ ,  $n^*$  and  $\alpha$  as well as their respective standard deviations when using different  $r$  filter absolute magnitude bin sizes. In addition, we display the number of bins that contain at least one identified cluster galaxy. It should be noted that we do not display the results of bin sizes that have fewer than five bins with identified cluster galaxies nor do we display the results of bin sizes that do not have successful fits.

This paper has been typeset from a  $\text{\TeX/L\AA\TeX}$  file prepared by the author.